A&A, 701, A60 (2025)
https://doi.org/10.1051/0004-6361/202554418

Astronomy & Astrophysics

New X-ray supernova remnants in NGC 7793

M. Kopsacheili[1,2,⋆], K. Anastasopoulou[3], R. Nanda[1,2], C. P. Gutierrez[2,1], and L. Galbany[1,2]

[1] Institute of Space Sciences (ICE, CSIC), Campus UAB, Carrer de Can Magrans, s/n, E-08193 Barcelona, Spain
[2] Institut d'Estudis Espacials de Catalunya (IEEC), 08860 Castelldefels (Barcelona), Spain
[3] Center for Astrophysics | Harvard & Smithsonian, 60 Garden Street, Cambridge, MA 02138, USA

Received 7 March 2025 / Accepted 5 June 2025

ABSTRACT

Context. This work focuses on the detection of X-ray supernova remnants (SNRs) in the galaxy NGC 7793 and the study of their properties.
Aims. X-ray SNRs in galaxies beyond the Local Group are rare, mainly due to the limited sensitivity of current X-ray instruments. Additionally, their identification requires an optical counterpart, making incomplete optical identification methods an extra challenge. Detecting X-ray SNRs in other galaxies is crucial to understanding their feedback in different evolutionary phases and gaining insights into their local interstellar medium (ISM). In NGC 7793, only one X-ray SNR was previously known, while a recent study reported nearly 240 optical SNRs. The discovery of a new, larger optical SNR sample motivated a re-examination of the X-ray SNR population by comparing optical SNRs with X-ray sources.
Methods. To identify X-ray SNRs, we utilised *Chandra*'s spatial resolution and analyzed all available archival data of NGC 7793, totaling 229.9 ks over 19 years. After data reduction, we performed source detection and analysis, searching for X-ray sources coinciding with optical SNRs. We also used *XMM-Newton* (1.1 Ms combined EPIC MOS) for a spectral analysis of the confirmed and candidate SNRs.
Results. We detected 58 X-ray sources down to an observed luminosity of $\sim 9 \times 10^{35}$ erg s^{-1}. Among them, five X-ray counterparts to optical SNRs were identified, all presenting soft emission (<1.2 keV) with no short- or long-term variability. One corresponds to the previously known X-ray SNR, while four are newly detected. Spectral modelling of two SNRs shows thermal spectra exceeding 2.5 million K, with strong O VII, O VIII, and Ne IX emission lines. A correlation between density, X-ray luminosity, and source softness was observed. We also report X-ray emission from supernova 2008bk, refining its position, and suggest two candidate X-ray SNRs with soft, non-variable spectra, one resembling the identified X-ray SNRs.

Key words. supernovae: individual: SN 2008bk – ISM: supernova remnants – X-rays: galaxies – galaxies: individual: NGC 7793

1. Introduction

Supernova remnants (SNRs) are very important galaxy components. They enrich the interstellar medium (ISM) with heavy elements and they depose to it large amounts of energy that heat and shape it. In addition, they can trigger star formation when their shockwaves compress nearby molecular clouds. Their systematic study can give information on their feedback to the ISM. In the case of core-collapse SNRs, they trace the massive-star formation rate of a galaxy, since those SNRs depict a massive star's end of life (e.g. Filippenko 1997).

The evolution of SNRs can be described by four consecutive phases: free expansion, adiabatic or Sedov-Taylor phase, radiative phase, and fade-out phase (e.g. Chevalier 1975; Cioffi et al. 1988). We usually observe SNRs in the Sedov-Taylor and radiative phases as they last longer, and during this time the SNRs' energetics reach their peak. In the first two phases, SNRs mostly emit in X-rays, where their fast shocks heat the ISM to temperatures of $\sim 10^7$ K, producing thermal emission. However, non-thermal emission can be produced from the central object, for example a pulsar or pulsar wind nebula (PWN), or, more rarely, in the SNR's shell because of relativistic particles accelerated by the shockwave. The optical emission is usually expected during the radiative phase (or at the end of the Sedov-Taylor phase), when the shock slows down and the SNR's temperature decreases. However, there are SNRs that are observed in both optical and X-rays, which probably indicates that they evolve in environments with high density variations. The portion of the SNR's shell that encounters denser ISM cools down and can produce optical emission lines, while the rest keeps moving at higher velocities, emitting in X-rays. There is another category of SNRs where optical (and/or radio) and thermal X-ray emission coexist. This is the mixed-morphology (or thermal composite) SNRs where the optical or radio emission comes from the shell and the X-ray emission from its central region. This category is not yet well understood; however, there are some explanations for its nature: (a) evaporating cloud in the interior of the SNRs may emit soft X-rays because of the evaporated material (Rho et al. 1994; White & Long 1991); (b) the SNR's shell collides with the density wall of a pre-existing cavity that has been formed by stellar winds of the progenitor star, and then a reflected shock reheats the SNR's interior, producing soft X-ray emission (Dwarkadas 2005; Chen et al. 2008; Zhang et al. 2015; Boumis et al. 2022); (c) the density in the interior of the SNR can be increased by thermal conduction, and the temperature also increases. The hot plasma emits in X-rays (Cox et al. 1999; Shelton et al. 1999). The most recent model was presented by Chiotellis et al. (2024), who proposed an SNR evolving in a cavity created by stellar winds of a massive-star progenitor. The forward shock encounters the density wall of the cavity, and then a reflected shock reheats the

⋆ Corresponding author: kopsacheili@ice.csic.es

supernova (SN) ejecta and the red supergiant bubble created during the last stage of the progenitor's life. There is another category of SNRs, (non-thermal) composite SNRs, that may present an optical/radio shell and non-thermal X-ray emission powered by a central object such as a neutron star. A multi-wavelength study of extragalactic SNRs is of high significance when it comes to understanding their feedback to the ISM and how ISM properties affect their evolution. The last decades, a lot of surveys have been published on Galactic SNRs and SNRs in Magellanic Clouds (MCs) at different wavelengths (e.g. Sasaki et al. 2006; Filipović et al. 2008; Milisavljevic & Fesen 2013; Maggi et al. 2019; Williams et al. 2020; Fesen et al. 2021; Boumis et al. 2022; Churazov et al. 2021,2022; Temim et al. 2022; Palaiologou et al. 2022; Albert & Dwarkadas 2022; Zangrandi et al. 2024). Their proximity allows the detailed investigation of their physical properties, morphological and kinematic characteristics, their interaction with their ambient medium, and their progenitor. Especially young SNRs, with prominent emission in X-rays, reveal information on the yields of the SN explosion and the circumstellar medium (CSM) or the ISM that is shaped by the progenitor (e.g. Vink 2012).

On the other hand, extragalactic SNRs provide the opportunity to study larger samples in various galactic environments, for example in galaxies with a different morphology, metallicity, or star formation rate (SFR). Optical studies have historically provided the highest number of extragalactic SNRs. Theoretical and observational studies in the optical, such as Leonidaki et al. (2013), Long et al. (2019), Cid Fernandes et al. (2021), Kopsacheili et al. (2021), and Kopsacheili et al. (2022), have revealed properties of SNR populations such density, shock velocities, and their connection to the ambient ISM. On the other hand, in other wavelengths the sample size is limited, primarily due to the sensitivity constraints of the instruments, especially in galaxies out of the Local Group (e.g. Fig. 13 in Leonidaki et al. 2013 and Fig. 7 in Bozzetto et al. 2017). Other studies have been dedicated to the simultaneous exploration of optical and X-ray or radio properties, such as Pannuti et al. (2007); Leonidaki et al. (2010); Pannuti et al. (2011); Winkler et al. (2021).

In this work, we used all the available archival *Chandra* data of NGC 7793 in order to seek new X-ray SNRs. NGC 7793 is a flocculent, spiral, almost face-on galaxy and member of the Sculptor Group (Puche & Carignan 1988), at a distance of 3.7 Mpc. It presents an SFR of $0.51\,M_{\odot}\,yr^{-1}$, based on the extinction-corrected Hα luminosity (Lee et al. 2009). Despite the large number of optical SNRs detected in galaxies beyond the Local Group, only a few X-ray SNR counterparts have been identified (e.g. Pannuti et al. 2007; Leonidaki et al. 2010). NGC 7793 is an excellent candidate for expanding the X-ray SNR sample, as it hosts many optical SNRs. While previous X-ray studies have reported a single X-ray SNR in this galaxy, the availability of new and larger optical SNR catalogues motivated us to revisit the search for additional X-ray SNRs.

In the optical, Blair & Long (1997) detected and spectroscopically confirmed 27 SNRs, based on the [S II]/H$\alpha > 0.4$ criterion. Two of them were also confirmed by Della et al. (2020). Later on, Kopsacheili et al. (2021) presented 55 candidate optical SNRs, 29 of which are new identifications, and more recently Kopsacheili et al. (2024) identified ~238 SNRs, ~225 of which are new identifications, based on multi-line diagnostics developed by Kopsacheili et al. (2020). In the radio, Pannuti et al. (2002) presented seven radio SNRs, two of which coincide with optical SNRs, while the rest of them were new identifications. More recently, Galvin & Filipovic (2014) presented a catalogue of 14 radio SNRs including five of the seven aforementioned radio SNRs. Two of them coincide with optical SNRs from the work of Blair & Long (1997). In X-rays, Pannuti et al. (2011) identified one SNR, which was a counterpart to the optical SNR S11 in Blair & Long (1997).

The structure of the paper is as follows. In Section 2, the X-ray observation details are presented, as well as the data reduction, the detection and analysis, and the hardness ratio calculation. In Section 3, we present our results, and in Section 4, we compare them to other studies. We also examine correlations between X-ray and optical properties. Finally, in Section 5, we summarise our results and draw our conclusions.

Table 1. Archival *Chandra* observations of NGC 7793 with ACIS-S.

OBS ID	Exp. (ks)	PI	RA (J2000)	Dec (J2000)	Start Date
3954	48.94	Pannuti	23:57:49.8	−32:35:29.5	2003-09-06
14231	58.84	Soria	23:57:59.9	−32:33:20.9	2011-08-13
13439	57.77	Soria	23:57:59.9	−32:33:20.9	2011-12-25
14378	24.71	Soria	23:57:59.9	−32:33:20.9	2011-12-30
23266	29.69	Walton	23:57:51.0	−32:37:26.6	2020-06-04
27481	9.95	Brightman	23:57:49.9	−32:35:27.7	2022-10-27

2. Observations and data analysis

2.1. Chandra data

In this work, we used *Chandra* (Weisskopf et al. 2000) archival data obtained by the ACIS-S camera (Garmire 1997) between 2003 and 2020, for a total exposure time of 229.9 ks. In Table 1, we present the details of each observation. The data analysis was performed using the `CIAO` software version 4.14 and `CALDB` version 4.9.7 (Fruscione et al. 2006).

We followed the standard *Chandra* analysis tools, and we started by running the *chandra_repro* script for each observation, which creates a new bad pixel file, and a level-2 event file. We also checked for background flares and found that the background was constant throughout the observations.

Before the detection process, with the aim of increasing the signal-to-noise ratio (S/N) of the X-ray sources of the galaxy, the observations were combined using the *merge_obs* tool, which first re-projects all the observations to a common target point and then creates a merged level-2 event file. We note that the merged observations are only used for the source detection and no other analysis. During this process, for each OBSID, images and exposure maps were produced in four bands: broad (0.5–7.0 keV), soft (0.5–1.2 keV), medium (1.2–2.0 keV), and hard (2.0–7.0 keV).

2.2. Source detection and fluxes

For the detection, we used the *wavedetect* tool (Freeman et al. 2002) and searched for sources in the broad, hard, medium, and soft images of the individual observations as well as of the merged one on scales of 1, 2, 4, 8, and 16 pixels. We then compared the outputs from all detections across bands and observations, and if a source appeared more than once, we retained it only once in the final source list.

In order to infer the count rates, for each detected source the PSF (Point Spread Function) that includes the 90% of the light in the broad band, was calculated using the *psfsize_srcs* tool. For the background, an annulus was defined with an inner

radius two pixels larger than the source aperture and outer radius double the size of that of the source aperture. This way, we avoided contamination from the wings of the source's PSF and ensured good count statistics. We visually inspected the source and background regions to avoid contamination from nearby sources. The source counts were extracted with the *dmextract* tool in the individual observations of the broad, soft, medium, and hard bands. The errors correspond to a 1σ Gaussian distribution. Since supernova remnants are expected to be predominantly soft and not variable over the time frame of the *Chandra* observations, fluxes were calculated using the OBSID with the highest S/N in the soft band. Combined observations were not used since the *Chandra* effective area, particularly at low energies, has changed over time due to contamination build-up on the ACIS optical blocking filter (e.g. O'Dell et al. 2015). This can introduce systematic errors in the derived fluxes when combining data from different epochs.

Fluxes were only calculated for a subset of sources (detailed in Section 4.7) for which we have indications of their nature, allowing us to apply appropriate spectral models. To do this, we used the *Chandra Proposal Planning Toolkit (PIMMS*[1]*)*. This tool allows the calculation of the flux of a source given its count rate in cases where the source count statistics do not allow for spectral extraction and modelling. The model and parameters used are detailed in that section[2].

2.3. Calculation of hardness ratios and colour-colour diagrams

Extragalactic SNRs usually are faint objects in X-rays. This does not allow for any meaningful spectral modelling and exploration of their spectral properties. In order to estimate the spectral properties of the X-ray sources, we calculated the hardness ratio of each detected source, which is usually the ratio of the counts of two bands or a monotonic function of it (Park et al. 2006). For the calculation of the hardness ratios, we used the Bayesian estimation of hardness ratios (BEHR; Park et al. 2006). This tool assumes Poisson distributions, a proper assumption in our case where most of the sources have low counts, and it evaluates the posterior probability distribution of the colours, providing reliable estimations and correct confidence limits, even for very low counts. In addition, it can estimate upper and lower limits in cases where a source is not detectable in one of the passbands.

We ran the BEHR code for the observation that presents the higher S/N in the soft band for each source, since we expected SNRs to present higher emission at lower energies. The hardness ratios that we used for the bands are as follows: soft-hard: $\log_{10}(S/H)$; soft-medium: $\log_{10}(S/M)$; and medium-hard: $\log_{10}(M/H)$, where soft, medium, and hard refer to the net counts with the energy ranges 0.5–1.2 keV, 1.2–2.0 keV, and 2.0–7.0 keV, respectively. The uncertainties of the hardness ratios were estimated at the 68% confidence level.

3. Results

We detected 58 X-ray sources, which are listed in Table A.1, along with their coordinates, the net count rates, and the S/Ns in the soft and broad bands. In Table B.1 of Appendix B, we present the selected OBSID of each source (i.e. the OBSID for which the S/N ratio in the soft band is higher) and the colours $\log_{10}(S/H)$, $\log_{10}(S/M)$, and $\log_{10}(M/H)$. In Figure 1, we show the composite X-ray optical image of NGC 7793 consisting of: Hα (red), soft X-ray (0.5–1.2 keV; green), and medium + hard X-ray (1.2–7.0 keV; blue). All circles indicate the X-ray detected sources. The orange circles show the X-ray sources that coincide with optical SNRs that have been identified in Kopsacheili et al. (2021) and Kopsacheili et al. (2024) and are the main focus of this study.

4. Discussion

4.1. Comparison of X-ray sources with other surveys

Of the 58 detected sources, 30 are reported for the first time in X-rays: X1, X2, X3, X4, X5, X6, X7, X8, X10, X16, X17, X20, X23, X24, X27, X29, X30, X31, X32, X35, X36, X37, X38, X44, X47, X48, X49, X51, and X55. Among these, 19 sources have S/N > 3, six have 2 < S/N < 3, and five have 1 < S/N < 2 (S/N in the broad band). From the remaining sources those that are unrelated to SNRs are compared with other surveys in Appendix C (and Table B.1). Subsequently, we talk about the detection of X-ray emission of the supernova 2008bk and then about sources that coincide with optical SNRs or could be associated with them.

Source X20 coincides with the hydrogen-rich SN 2008bk, and it only appears in the *Chandra* observations after 2008. SN 2008bk is a low-luminosity SN II-P (e.g. Van Dyk et al. 2012). Its progenitor is a red supergiant with an initial mass of $\sim$13 $M_\odot$ (Maund et al. 2014), while a mass of $\sim$8.5 $M_\odot$ had previously been reported (Mattila et al. 2008; Van Dyk et al. 2012). In Figure 2, we show observations of that region in 2003 on the left, observations in 2011 with *Chandra* in the middle, and an inverted-colour Hα+[N II] image from the Blanco 4 m telescope (MOSAIC II camera) obtained in 2011 on the right. In the latter, we can also see the light echo around it (Van Dyk 2013). We note that during this phase we observe the SN 2008bk in both *Chandra* and optical data at an offset of 1.7 arcseconds compared to the position reported by Li et al. (2008). Hence, we refine its position and the new coordinates, which are RA: 23h57m50.5s and Dec: −32d33m20.3s.

The interaction between the SN ejecta and CSM can produce X-ray emission, as observed in the hydrogen-rich SN 1979C (e.g. Chevalier 1982). Recent radiative transfer simulations of hydrogen-rich SNe (Type II SNe) further illustrate how interaction-driven power influences their optical spectra at late phases (>1000 days). These simulations suggest that interaction primarily enhances flux in the ultraviolet, and, if the shock power is not fully thermalised, the SN should exhibit significant X-ray luminosity (Dessart et al. 2023).

Although SN 2008bk appears very faint in the *Chandra* observations, we detect it in all the observations of 2011, i.e. in the OBSIDs: 14231, 13439, and 14378, with the highest S/N (in the broad band) in that of 14231, where S/N = 2.76. We do not detect the SN 2008bk in later observations, most probably because of the significantly shorter exposure time. Because of the faintness of the supernova, we could not extract any spectra using *Chandra* observations. Hence, we used PIMMS to estimate the flux. To do that, we considered i) a thermal emission model with $kT = 1.5$ keV (e.g. Pooley et al. 2002) and ii) a power law with an index of 1.9 (e.g. Misra et al. 2007). The

[1] https://cxc.harvard.edu/toolkit/pimms.jsp

[2] A similar analysis could, in principle, be performed using information from the Chandra source catalogue (Evans et al. 2010). However, one of the observations is not included in the latest CSC release (v2.1). In order to ensure consistency and to apply SNR-appropriate models, we reanalysed the data.

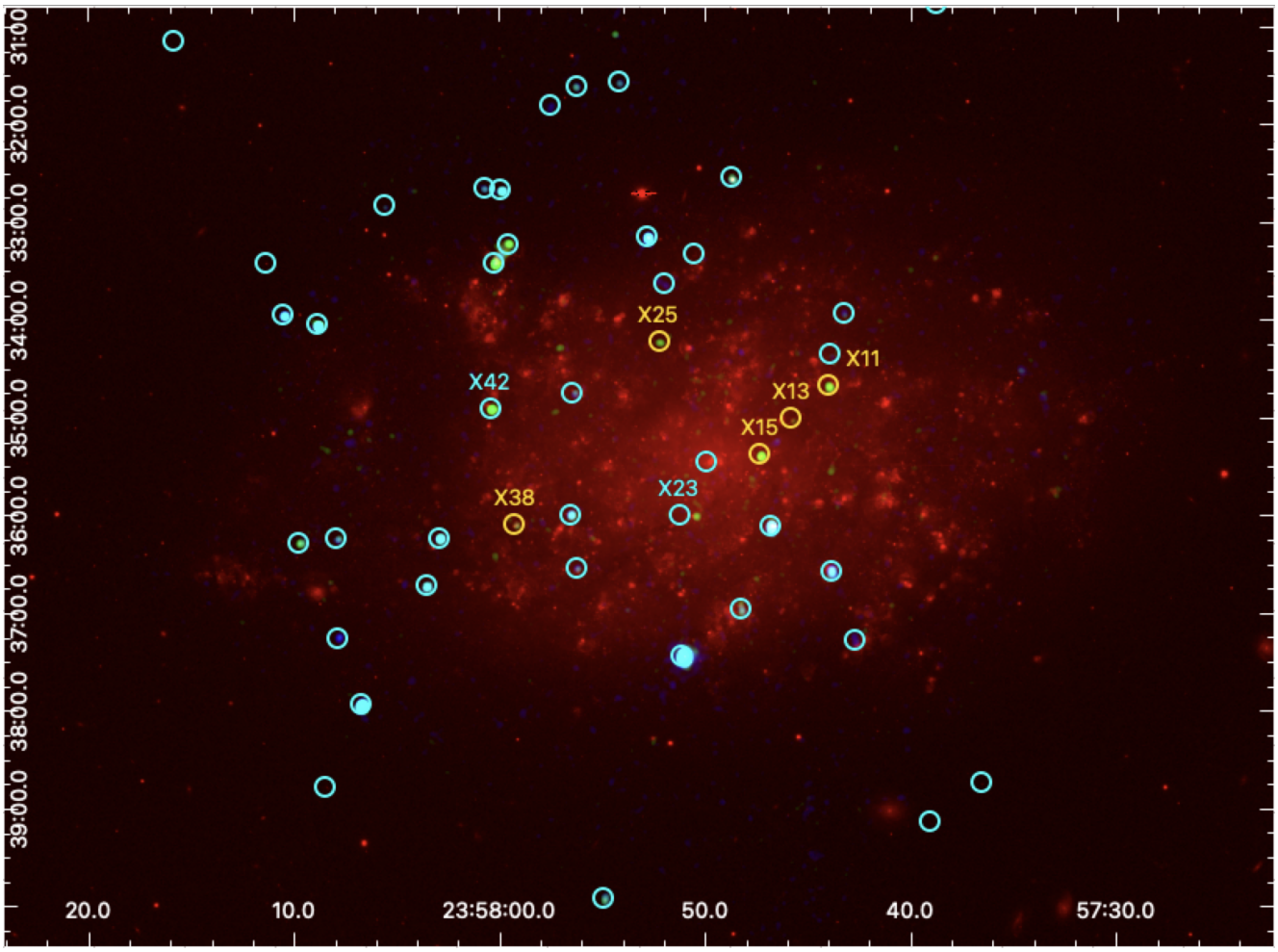

Fig. 1. Composite X-ray optical image of NGC 7793 consisting of Hα + [N II] (red), soft X-ray (0.5–1.2 keV; green), and medium + hard X-ray (1.2–7.0 keV; blue) of the OBSID 3954. All circles indicate the X-ray detected sources. The orange circles show the X-ray sources that coincide with optical SNRs that have been identified in Kopsacheili et al. (2021) and Kopsacheili et al. (2024).

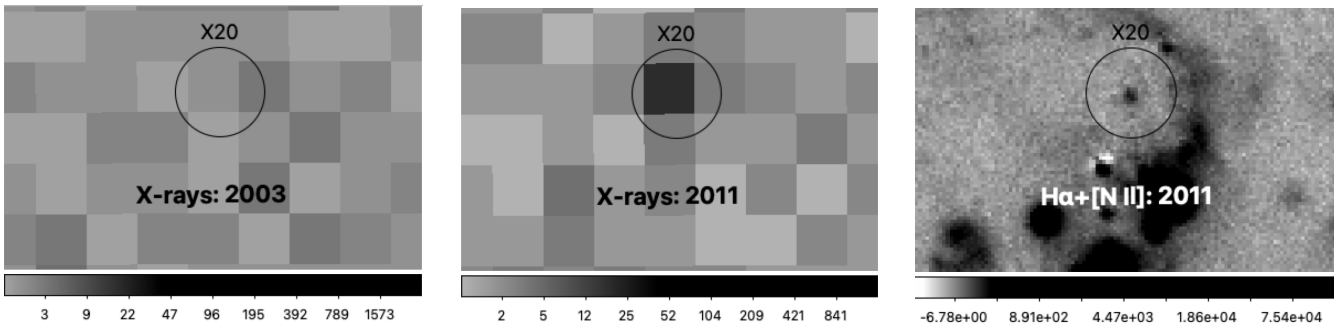

Fig. 2. Source X20 is SN 2008bk. In the left and middle panels, we see the *Chandra* images from 2003 (OBSID: 3954) and 2011 (OBSID: 14231), respectively, in the broad band (0.5–7 keV); on the right we see the continuum-subtracted Hα+[N II] image from the Blanco 4 m telescope (MOSAIC II camera) obtained in 2011. In all figures, the radius of the circle is 3.5 arcsec.

fluxes are $(1.21 \pm 0.32) \times 10^{-15}$ erg s^{-1} cm^{-2} and $(2.37 \pm 0.63) \times 10^{-15}$ erg s^{-1} cm^{-2} for the two models, respectively.

4.2. X-ray sources known or suspected as SNRs

In this section, we compare the detected X-ray sources with known or suspected as SNRs from other studies. Sources X11, X13, X15, X25, and X38 coincide with optical SNRs, and hence this analysis focuses on them. Among those, only X15 has been detected before and is a known X-ray SNR.

Source X14 (CXOU J235746.7-323607 in Pannuti et al. 2011) is the X-ray counterpart to the candidate radio SNR R3 Pannuti et al. 2002). This source was presented earlier as P10 by Read & Pietsch (1999), which suggested that its soft, X-ray spectrum comes from a super-bubble or multiple SNRs. However, P10 has an offset of 6″ in relation to source X14; hence, they are probably two different physically associated sources. Pannuti et al. (2011) reported that its time variability rejects the single-SNR scenario and it may be an SNR/XRB system analogous to the Galactic source W50/SS 433 (Safi-Harb & Petre

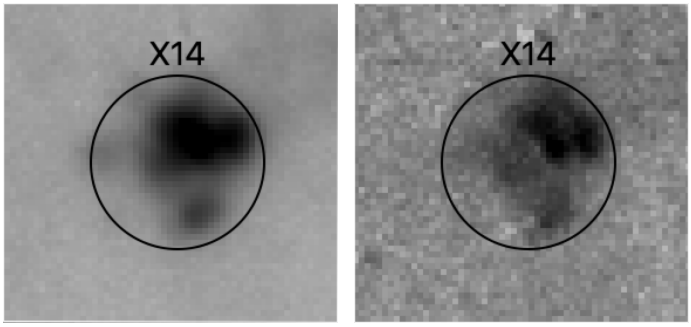

Fig. 3. Optical counterpart of the source X14 in Hα + [N II] (left) and [S II] (right). The optical images were obtained from the Blanco 4m telescope (MOSAIC II camera) in 2011.

1999), where synchrotron emission results from the collision between the jets from the microquasar SS 433 and the surrounding SNR (W50) shell. In Figure 3, this source in Hα+[N II] and [S II] from MOSAIC II camera on the Blanco 4 m telescope (Chile) are presented. The [S II]/Hα ratio is ∼0.15 (calculated using the photometry presented in Kopsacheili et al. 2021), and it does not satisfy the traditional diagnostic to class it as an SNR, according to which this ratio is higher than 0.4 for SNRs. In order to explore if this is indeed an optical SNR, other diagnostics that require more emission lines or spectra are needed (e.g. Kopsacheili et al. 2020). However, as can be seen in Figure 3, there are multiple 'peaks', perhaps indicating that there are more sources there. A contaminating source, bright in Hα, would lead to lower [S II]/Hα ratios, or other ratios indicative of shock excitation, even if there is an SNR there. Finally, it could be a young SNR, the shock velocity of which (and thus temperature) is too high to produce strong optical emission lines, such as [S II] and [N II]. In order to be conservative, we did not consider X14 as SNR.

Source X9 coincides with the source CXOU J235743.8-323633 in Pannuti et al. (2011). It has an offset of 2.5″ from the H II region D22, which was reported in Davoust & de Vaucouleurs (1980) (D22). Pannuti et al. (2011) suggested that it can be either an SNR or a X-ray binary associated with the H II region. X9 does not present any emission in the optical, and it is close to the edge of a large, ring-like structure that has not been identified as SNR. Hence, at this point, we do not classify X9 as an SNR.

X15 has been identified as an optical SNR in Blair & Long (1997; S11), in Kopsacheili et al. (2021; 7793_22), and in Kopsacheili et al. (2024; NGC7793_SNR_136), as a radio SNR in Pannuti et al. (2002; N7793-S11), and X-ray SNR in Pannuti et al. (2011; CXOU J235747.2-323523). Sources X11 and X13 coincide with the optical SNRs 7793_24 and 7793_23 in Kopsacheili et al. (2021) and NGC7793_SNR_91 and NGC7793_SNR_126 in Kopsacheili et al. (2024). Source X25 (J235752.2-323413 in Pannuti et al. 2011) coincides with the optical SNR 7793_5 in Kopsacheili et al. (2021), and X38 with the S24 in Blair & Long (1997) and 7793_21 in Kopsacheili et al. (2021). In the study of Mineo et al. (2012), the sources X11 and X25 are presented as J235743.9-323441 and J235752.2-323413, respectively, and they are reported to reside in areas dominated by a high-mass X-ray binary (HMXB) population. The offset of X11, X13, X15, X25, and X38 from the optical SNRs are 0.7, 1.3, 1.3, 0.4, and 0.6 arcseconds, respectively. The coordinates of the optical SNRs were taken from Kopsacheili et al. (2024; X11, X13, X15) and Kopsacheili et al. (2021; X25, X38).

4.3. X-ray colours

We further examined the properties of X11, X13, X15, X25, and X38, which coincide with optical SNRs, in order to decide if they should indeed be considered as X-ray SNRs. The most accurate way to do so, is to examine their X-ray spectra. X-ray SNRs present thermal emission from shock-heated plasma, and sometimes young SNRs' non-thermal emission from relativistic electrons moving in the magnetic fields of hot plasma. The thermal emission is often characterised by emission lines of O, Ne, Mg, Si, S, Ar, Ca, and iron-group elements (e.g Vink 2020). However, the faintness of SNRs at distances, such as NGC 7793, usually does not allow the extraction of a detailed spectrum where emission lines can be observed, and hence no emission lines are present.

In such cases, colours or hardness ratios are a good proxy to quantitatively characterise a spectrum. In this study, we calculated the colours log(S/M), log(S/H), and log(M/H), as described in Section 2.3. Then, the colour-colour diagrams log(S/M) − log(S/H), log(S/M) − log(M/H), and log(S/H) − log(M/H) were constructed and are presented in Figure 4. All the data points refer to the X-ray sources with S/N > 1 in the soft band. Orange squares are the X-ray sources X11, X13, X15, X25, and X38, which coincide with optical SNRs, while the star is the SN2008bk (X20). As can be seen, although the error bars are large, in all three plots the orange squares occupy the soft part of the diagrams. This is the region where X-ray SNRs are expected since they are characterised by temperatures of up to $\sim 10^7$ K.

4.4. New X-ray SNRs

In this study, we detected X-ray sources in the galaxy NGC 7793 and found that five of them (X11, X13, X15, X25, X38) coincide with optical SNRs (one is a known X-ray/radio SNR) with offsets smaller than 1.3 arcsec. The X-ray colours of these sources present soft or super-soft emission, which is expected from SNRs.

We examined the probability of these sources presenting long or short variability. For the long variability, we compared the photometry of the different observations where these sources have been detected, and we found that it is stable within the uncertainties. For the short-variability check, the `glvary` tool of the `CIAO` software was used. This tool looks for significant deviations among multiple time bins of the events using the Gregory-Loredo algorithm. Among the output values, the probability of the examined source being variable is given. If the variability index that returns the `glvary` is less than three, we can consider our sources as non-variable. All of the five sources we examined gave a variability index less than or equal to two. More specifically, those are 1, 0, 0, 1, and 2, for X11, X13, X15, X25, and X38, respectively. No variability is expected from SNRs, so the lack of variability observed in these sources enhances the SNR scenario.

Concluding, X11, X13, X25, X38 can be considered as new X-ray SNRs joining the known SNR X15. For consistency and comparison reasons, in the following analysis we included the SNR X15, although it is a known X-ray SNR (Pannuti et al. 2011). These X-ray SNRs had not been presented before because (a) they were not detected in other X-ray studies (in this study, we ran the detection on individual and combined observations, increasing the S/N); and/or (b) no optical/radio identification had been reported before (the absence of which makes identification as an X-ray SNR very uncertain).

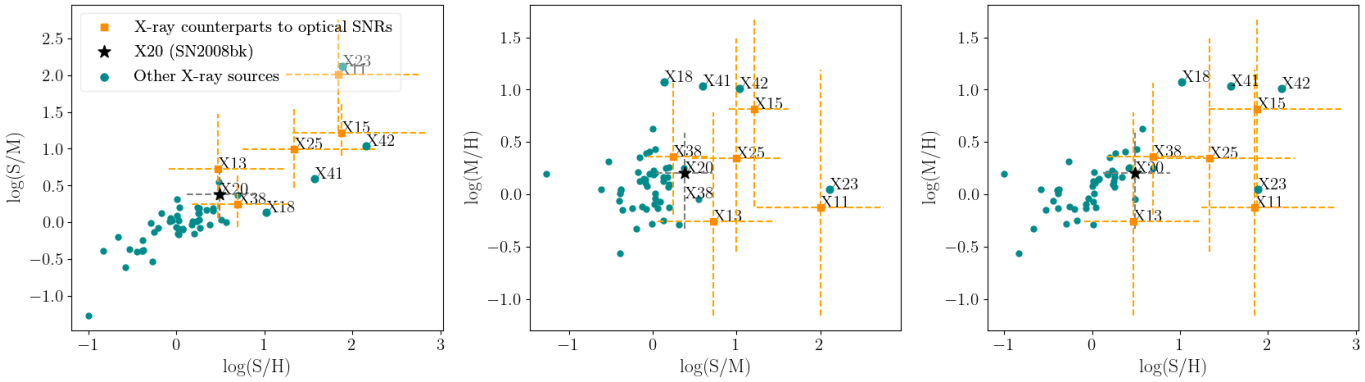

Fig. 4. $\log_{10}(S/M) - \log_{10}(S/H)$, $\log_{10}(M/H) - \log_{10}(S/M)$, and $\log_{10}(M/H) - \log_{10}(S/H)$ X-ray colours for all the X-ray-detected sources with S/N > 1, detected in this work. The orange squares correspond to the X-ray sources that coincide with optical SNRs.

4.5. Candidate X-ray SNRs without optical counterpart

In Figure 4, apart from X11, X13, X15, X25, and X38, there are more sources that fall in the soft part of the colour-colour diagram. Those are X18, X23, X41, and X42. We examine these sources in order to decide if they could be considered as candidate SNRs. X18 is the foreground star P6 (Read & Pietsch 1999, Monet et al. 2003, Pannuti et al. 2011) that had earlier been misclassified as an H II region (H18; Hodge 1969). X41 is a microquasar, as discussed in Section C (Pakull et al. 2010, Soria et al. 2010). Around the microquasar there is a super-bubble (e.g. Kopsacheili et al. 2021), the emission properties of which are similar to those of an SNR; that is why it was initially misclassified as an SNR (S26 in Blair & Long 1997).

X23 (detected for the first time in this study) and X42 have not previously been classified, but they have been reported near regions dominated by X-ray binaries (Mineo et al. 2012). They appear in the soft part of the color-color diagrams (Figure 4), and they do not present any variability. Putting everything together, we do not have any strong evidence against the scenario of X23 and X42 being SNRs, and hence we can consider them candidate SNRs. The reason we do not detect any optical emission could be an implication of a low-density environment, where no bright optical emission is produced. This in turn could imply an SN Ia origin (e.g. Winkler et al. 2021).

4.6. X-ray spectral analysis of SNRs and candidate SNRs

Sources that are described in the previous sections as known or candidate SNRs (X11, X13, X15, X23, X25, X38, X42) are very soft and have very few counts in the *Chandra* data, not allowing for spectral modelling. While the *Chandra* X-ray colours offer valuable insights into the spectral properties of the sources, we aimed to take this a step further by extracting spectra from archival *XMM-Newton* observations. This approach allowed us to take full advantage of *Chandra*'s high spatial resolution for precise source positions, while leveraging *XMM-Newton*'s large effective area and better sensitivity at soft energies to maximise the spectral information obtained from these sources. To put this into perspective, the brightest of these sources, X15, a known SNR, has approximately 99 combined net counts with *Chandra*, while the combined EPIC MOS net counts exceed this by more than six times (reaching around 600), allowing for detailed spectral modelling with χ^2 square statistics.

We used 14 *XMM-Newton* observations (listed in Table 2) that covered the sources without contamination from any nearby outbursting sources. For the standard calibration of the observations, we utilised the *XMM-Newton* science analysis system (SAS) v19.0.0 and obtained filtered event files clean of background flares, as described in detail in Haberl et al. (2012) and Anastasopoulou et al. (2023). During this study, we only used the EPIC MOS detectors, which offer a combined clean exposure time of ~1.1 Msec. Although the PN detector offers higher sensitivity, we found that the combined MOS spectrum provided comparable S/N and lower background noise, particularly at soft energies (<1 keV), allowing clearer detection of the spectral emission lines.

We extracted the source spectra for each OBSID MOS detector using the *evselect* SAS task, centring the extraction regions on the *Chandra* source coordinates. The extraction regions were carefully chosen to enclose at least 80% of the PSF while minimising contamination from nearby sources. The background regions were placed in source-free areas near the targets and were sufficiently large to ensure an adequate number of counts in each observation. We then extracted the auxiliary response files (ARFs) for the source spectra and the redistribution matrix files (RMFs) using the SAS tasks *arfgen* and *rmfgen,* respectively. The background area was calculated using the *backscale* SAS task.

Table 2. *XMM-Newton* observations of NGC 7793 utilised in this study.

OBS ID	Exp MOS1 sec	Exp MOS2 sec	Start date
0693760401	47617	47585	2013-11-25
0748390901	48649	48620	2014-12-10
0804670301	54885	55063	2017-05-20
0804670401	32170	32513	2017-05-31
0804670501	32910	32991	2017-06-12
0804670601	31095	31117	2017-06-20
0804670701	51643	51618	2017-11-25
0823410301	25938	26078	2018-11-27
0823410401	26587	26572	2018-12-27
0853981001	41669	42373	2019-05-16
0840990101	38269	38716	2019-11-22
0861600101	67413	67666	2020-06-27
0883780101	40524	40573	2021-05-29
0883780201	30476	33721	2021-11-20

Notes. Exposure times correspond to clean exposures after the removal of time periods with high background flares.

Table 3. *XMM-Newton* spectral modelling.

Name	$N_{\rm H}^{\rm local}$	kT	norm	χ^2_ν (χ^2/d.o.f.)	$F_{\rm X}$	$F_{\rm X}^{\rm ISMcor}(F_{\rm X}^{\rm cor})$	$L_{\rm X}$	$L_{\rm X}^{\rm ISMcor}(L_{\rm X}^{\rm cor})$
	10^{22} cm^{-2}	keV	10^{-4}		10^{-15} erg cm^{-2} s^{-1}	10^{-15} erg cm^{-2} s^{-1}	10^{36} erg s^{-1}	10^{36} erg s^{-1}
(1)	(2)	(3)	(4)	(5)	(6)	(7)	(8)	(9)
				XSPEC model: *tbabs*×*phabs* × ∑*vapec*				
X11	$0.48^{+0.35}_{-0.30}$	0.13 ± 0.04	$1.5^{+102.0}_{-1.5}$	1.19 (58.69/49)	$3.35^{+0.01}_{-3.35}$	3.96 (5.05)	$5.49^{+0.01}_{-5.49}$	6.49 (8.27)
X15	$0.46^{+0.34}_{-0.24}$	<0.12	$8.5^{+58}_{-8.1}$	0.95 (50.51/53)	3.92 ± 1.8	4.38(32.7)	6.42 ± 2.94	7.17 (53.6)
		$0.78^{+0.09}_{-0.13}$	$0.03^{+0.02}_{-0.01}$					
X42[a]	$0.21^{+0.30}_{-0.19}$	0.23 ± 0.04	$0.09^{+0.42}_{-0.05}$	1.32 (68.89/52)	$3.87^{+0.01}_{-3.60}$	4.36 (9.71)	$6.34^{+0.41}_{-5.89}$	7.14(15.8)

Notes. In Column 1, we provide the name of the source spectrum. Columns 2 to 4 list the best-fit component values: the local absorption and the temperature of the thermal plasma and its normalisation, respectively. The Galactic column density towards NGC 7793 is fixed to a value of 3.4×10^{20} atoms cm^{-2}. The normalisation of the thermal component is expressed in units of $\frac{10^{-14}}{4\pi D^2} \int n_{\rm e} n_{\rm H}\, dV$, where $n_{\rm e}$ and $n_{\rm H}$ are the electron and hydrogen densities, respectively, integrated over the emitting region's volume, V, and D represents the source distance in centimetres (Smith et al. 2001). In Column 5, we present the values of the χ^2 statistic. Columns 6 and 7 provide the absorbed 0.5–7.0 keV flux and the corrected values (for only the ISM and total absorption), respectively. Columns 8 and 9 contain the corresponding luminosity values. Errors are quoted at the 1σ confidence level. The adopted distance to NGC 7793 is 3.7 Mpc. [(a)] The abundances of the following elements were left free to vary: Ne = $2.21^{+1.27}_{-0.88}$, Mg = $2.94^{+4.08}_{-2.78}$; a Gaussian line was added to the model with the best-fit parameters LineE=1.03 ± 0.02 keV and norm = $(1.66^{+1.29}_{-1.11}) \times 10^{-7}$.

To maximise the S/N, we combined all MOS spectra using the SAS task *epicspeccombine*, which generates a combined source spectrum, background spectrum, and response file. To fit the spectra, we used the XSPEC v.12.13.0c software (Arnaud 1996) and two models typically used to fit the shock-heated plasma that produces the X-ray emission in SNR spectra, namely the `vapec` and `vpshock` models. The model `vapec` corresponds to collisionally ionised diffuse gas in thermal equilibrium, while the `vpshock` model is a constant temperature plane-parallel shock plasma model that allows for non-equilibrium. Both models provide the possibility of varying the abundances. In order to allow for χ^2 statistics during the X-ray spectral fitting process, we grouped the data in bins of at least 20 total counts. We used a model of the form `tbabs`×`phabs`× ∑`model`, where `model` corresponds to either the `vapec` or the `vpshock` model. The `tbabs` component was used to model ISM absorption, with its value fixed at 3.4×10^{20} atoms cm^{-2} – the weighted average absorption towards NGC 7793. The second absorption component, `phabs`, was allowed to vary to account for local ISM absorption fluctuations or absorption intrinsic to the SNR. In all cases, we adopted the abundance table from Wilms et al. (2000), as it is the most up-to-date reference for use with the `tbabs` model.

We successfully extracted and modelled spectra for sources X11, X15, and X42. However, sources X25 and X38 were too faint for spectral modelling, while sources X13 and X23 were located near other X-ray sources, making it impossible to disentangle their emission. In Table 3, we only present only the results for the `vapec` model for sources X11, X15, and X42, since the `vpshock` model yielded results consistent with a plasma near equilibrium. For source X42, we thawed the Ne and Mg abundances and included an additional Gaussian component (`gauss`) at 1.03 keV to better account for the emission lines present in the spectrum. We present the best-fit parameters along with the corresponding fluxes and luminosities, with uncertainties given at the 1σ level. We present the combined *XMM-Newton* MOS spectra along with their best-fit models in Figure 5.

All sources are soft emitters with no detected emission above 2 keV, and their absorption components agree within the uncertainties, suggesting similar conditions at their locations. The spectra exhibit strong emission lines from K-shell transitions of various elements, indicating a thermal plasma with temperature exceeding 2.5×10^6 K. Specifically, in X11, we detect prominent emission lines of O VII (~0.55 keV), O VIII (~0.65 keV), and Ne IX (~0.9 keV). In X15, we observe O VII (~0.55 keV) and Ne IX (~0.9 keV), while in X42, O VIII (~0.65 and 0.85 keV) and Ne IX (~1.05 keV) are present.

Source X11 is well fitted with a single soft thermal component at $kT = 0.13$ keV. In contrast, a single thermal component did not provide a good fit for source X15, yielding $\chi^2_\nu \approx 2.0$. Instead, the best-fit model required two thermal plasma components: a soft component with $kT < 0.12$ keV and a harder component at $kT = 0.78$ keV. Source X42 is well described by a single thermal component at $kT = 0.19$ keV, though residuals remain at ~1.5 keV (Ne IX).

Over the eight years of available *XMM-Newton* observations, we detect no long-term variability, which is consistent with expectations for SNRs. The low temperatures ($kT < 0.78$ keV) of the best-fit spectra (Table 3) suggest that these are relatively old SNRs. This is also supported by the fact that they exhibit strong optical emission.

4.7. Exploring correlations with optical properties

X-ray SNRs are usually young SNRs, where shock velocities are very high and heat the ISM to temperatures of 10^7 K, producing thermal X-ray emission. On the other hand, optical emission, especially from forbidden lines, such as [S II] and [N II] is expected mainly from more evolved SNRs, where the temperature has dropped to ~10^4 K. The presence of both thermal X-ray and optical emission is probably an indication of a non-uniform or very dense environment. For example, a highly non-uniform environment may permit a part of the SNR to expand with high velocity, emitting in X-rays, while another part of the shock, evolving in a denser environment, may have already entered the radiation phase. Another scenario of both optical and X-ray emission in SNRs can be the case of mixed-morphology SNRs, where optical or radio emission is observed from the shell, while thermal X-ray emission is observed from the centre. This kind of SNR requires a dense environment (e.g. Chiotellis et al. 2024). The lack of spatial resolution in the study of galaxies outside of the Local Group prevents us from examining the aforementioned scenarios.

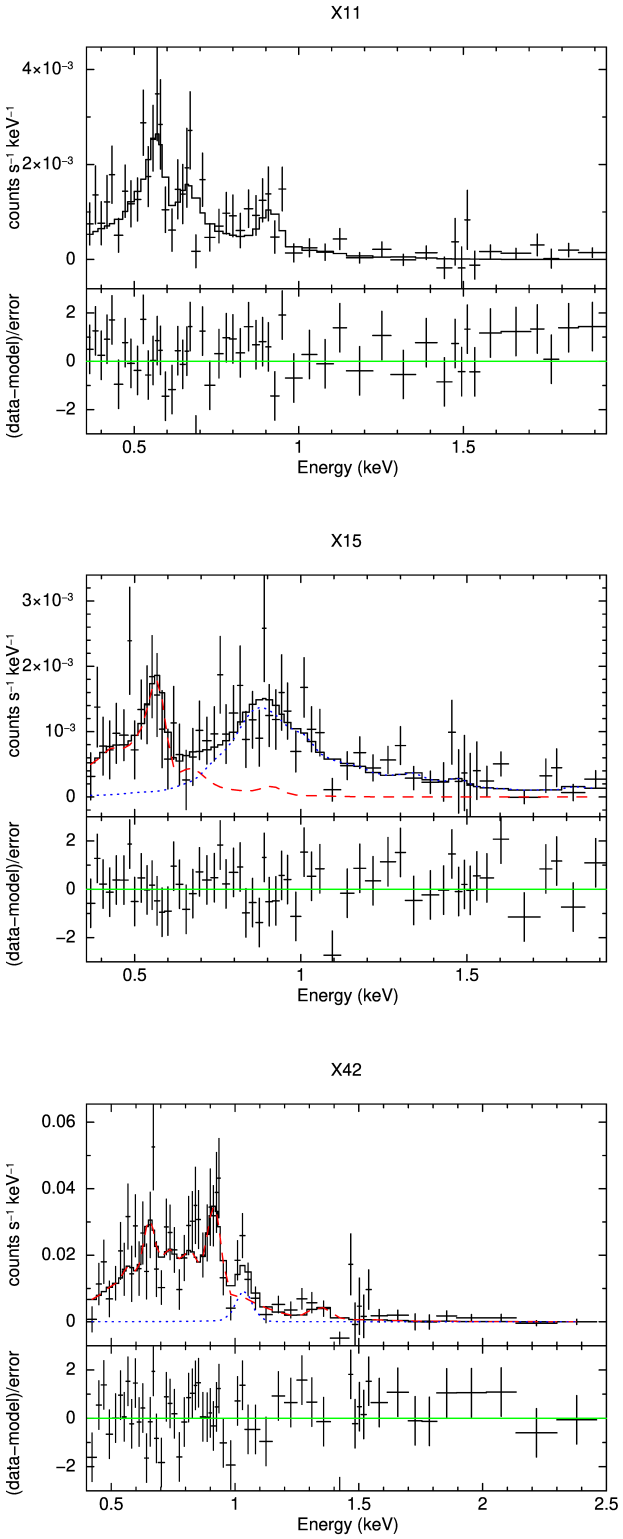

Fig. 5. Combined EPIC MOS spectra and best-fit models for sources X11, X15, and X42. The spectra of X11 and X42 are fitted with one temperature thermal-plasma model. The spectrum of X15 is fitted with two temperature thermal-plasma components shown with red dashed and blue dotted lines. The fit residuals for all sources are displayed in the bottom panels of each plot, with error bars representing 1σ uncertainties.

Subsequently, we examined possible correlations between X-ray and optical properties of SNRs. In order to account for the instrument's characteristics (e.g. effective area), we chose to perform the comparisons using X-ray luminosities rather than raw count rates. However, spectral fits are only available for two out of the five SNRs (Figure 5), for which the kT and $N_{\rm H}$ parameters have been determined. For the remaining SNRs, we assumed $kT = 0.5$ keV, a typical value for a thermal bremsstrahlung model for SNRs (e.g. Leonidaki et al. 2010), and $N_{\rm H} = 0.504 \times 10^{22}$ cm^{-2}, the average of the total $N_{\rm H}$ values for X11 and X15 in Table 3 (Galactic + local). We only chose X11 and X15 (and not X42), because they exhibit optical emission, and we expect similar properties for the also optically detected X13, X25, and X38. Given that unabsorbed fluxes are highly model-dependent, and small deviations from the true values of kT and $N_{\rm H}$ can result in significantly different estimates, we used and present the observed fluxes rather than those corrected for local and Galactic extinction. The fluxes were calculated using the PIMMS tool (detailed description in Section 2.2). The observed luminosities, along with other relevant properties, are listed in Table 4. For the calculation of the luminosity, and throughout this study, we adopted a distance of 3.7 Mpc (Radburn-Smith et al. 2011).

We explored the relation between X-ray emission and colours with the Hα luminosity; the emission line ratios [S II]/Hα, [N II]/Hα, and [O III]/Hβ (these ratios are indicative of the shock excitation of the gas); and the densities that were calculated using the ratio [S II](6717)/[S II](6731). The main idea behind the use of the [S II] ratio for the density estimation is that the collisional excitation from lines from the same ions, with more or less the same excitation energy, is proportional to the collision rates, and hence their ratio is a density indicator (e.g. Osterbrock & Ferland 2006; Draine 2011). Due to the lack of an optical spectrum of X25, the density was not calculated. In Table 4, all these properties are presented. The Hα flux and the optical emission-line ratios of X11, X13, and X15 were obtained from Kopsacheili et al. (2024), those for X25 from Kopsacheili et al. (2021), and those for X38 from Blair & Long (1997), where they present spectroscopic fluxes and ratios. We note here that for the latter, the [O III] and [N II] emission includes emission from the 4959Å + 5007Å and 6548Å + 6584Å lines, respectively, while for the rest of the cases the emission comes from [O III](5007) and [N II](6583).

X11, X13, and X15 are the X-ray counterparts of NGC7793_SNR_91, NGC7793_SNR_126, and NGC7793_SNR_136, from the study of Kopsacheili et al. (2024), the optical spectra of which are presented in Figure 6. Spectral fluxes of X38 are also available in the work of Blair & Long (1997). A common characteristic that we observe in the four of them is the strong [O III] emission. Not all the SNRs present [O III] emission. For example, in the work of Kopsacheili et al. (2024), only ~35% of the sample presents [O III] emission. This is most probably an indication that the shock velocity of these SNRs cannot be very low (e.g. Raymond 1979). However, no correlation seems to exist between [O III]/Hβ and X-ray luminosity or colour.

Exploring all the parameters, we find a possible correlation between density and luminosity, and density and $\log_{10}$(S/H), according to which luminosity and colour increase with the density. Both tendencies can be seen in Figure 7. Although the sample is very small, only four points, we applied a weighted Pearson correlation test (a method to measure a linear correlation between two variables, and weighted to take into account the uncertainties in luminosity and colour) in order to examine if there is indeed any linear correlation and if this can be random or not. The results are presented in Table 5. Both relations show a correlation of around 0.9. However, the hypoth-

Table 4. Optical and *Chandra* X-ray properties of the X-ray SNRs.

ID	L_X ($\times 10^{36}$ erg s^{-1})	$\log_{10}$(S/H)	$L_{H\alpha}$ ($\times 10^{36}$ erg s^{-1})	[S II]/Hα	[N II]/Hα	[O III]/Hβ	Density (d) (cm^{-3})
X11	$5.49^{+0.01}_{-5.49}$	$1.84^{+0.92}_{-0.6}$	15.0 ± 0.05	0.71	0.46	7.08	620.96
X13	0.88 ± 0.45	$0.47^{+0.78}_{-0.56}$	11.0 ± 0.05	1.07	0.5	2.45	6.72
X15	6.42 ± 2.94	$1.88^{+0.96}_{-0.56}$	6.6 ± 0.03	1.15	0.6	1.82	483.97
X25	1.79 ± 0.26	$1.34^{+0.96}_{-0.59}$	1.6 ± 0.05	0.66	–	–	–
X38	1.49 ± 0.47	$0.69^{+0.58}_{-0.52}$	23.0 ± 0.4	0.61	0.43	2.97	196.11

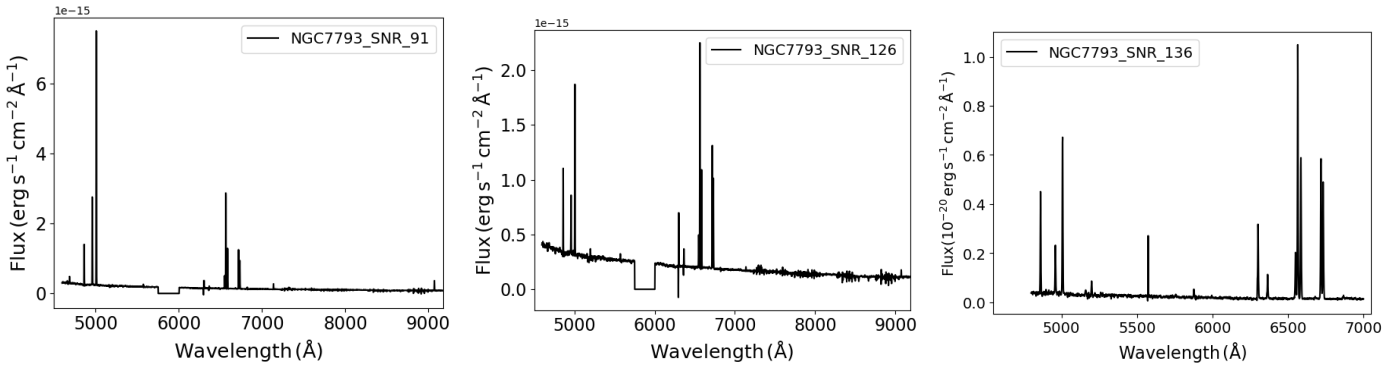

Fig. 6. Optical spectra of NGC7793_SNR_91, NGC7793_SNR_126, NGC7793_SNR_136, and optical SNRs that spatially coincide with the X-ray sources X11, X13, and X15 of this study.

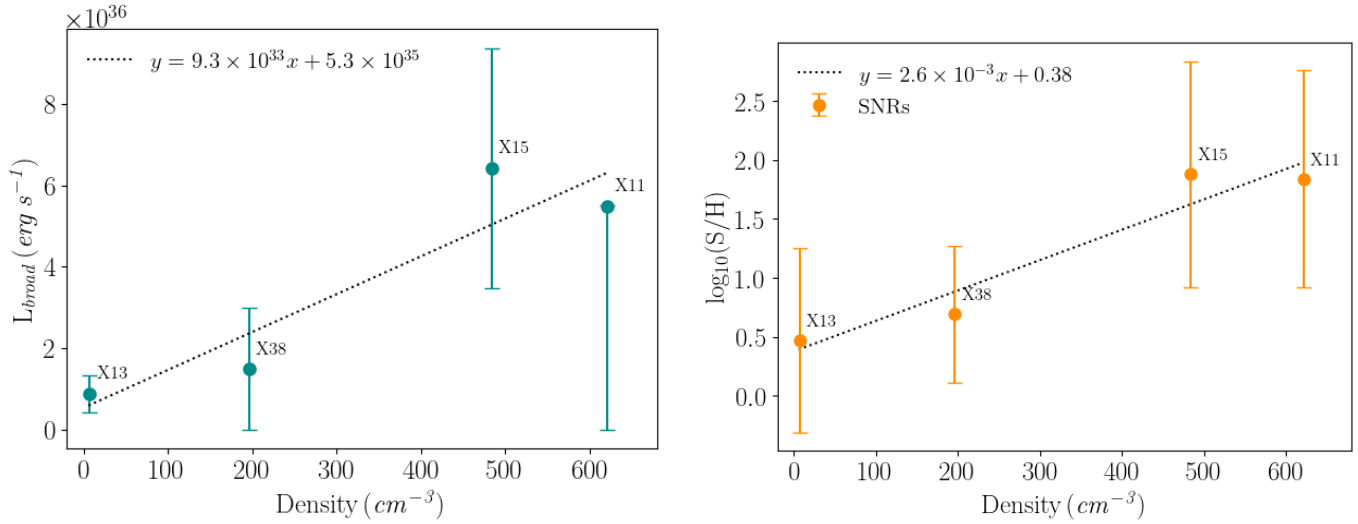

Fig. 7. *Left:* X-ray luminosity in the broad band (0.5–7 keV) of the X-ray SNRs X11, X13, X15, and X38 as function of their density, calculated using the [S II]6717/31 emission-line ratio. *Right:* $\log_{10}$(S/H) colour of the same sources, as function of the density. In both cases, the best-fit line is shown.

esis of this correlation being random cannot be excluded, as indicated by the relatively high p values. More specifically, the probability of this association being random is 40% for the luminosity-density relation and 14% for the colour-density relation.

The increase of the X-ray luminosity with the density is theoretically expected. The X-ray and optical emission are related to the shock emissivity, which is proportional to the square of the density. If we had more sources, we could perhaps see a more quadratic than linear relation. In our case, the X-ray emission is dominated by the soft emission, and for this reason the colour $\log_{10}$(S/H) is always positive. Hence, similar behaviour to that of the luminosity is expected for the relation $\log_{10}$(S/H)-density. Since both X-ray and optical emissions depend on the shock emissivity, a correlation between those two would be reasonable. However, such a correlation is not observed (Figure 8). The absence of a correlation between Hα and X-ray emission is also observed in the study of Pannuti et al. (2007), which compared the Hα luminosity of nine optically identified SNRs in M101 and NGC 2403 with the X-ray luminosity of *Chandra*-detected counterparts. The authors explained that this probably happens because of a non-uniform ambient that requires more complex emissivity models to be properly described. Leonidaki et al. (2013) reached a similar conclusion in their study of 16 optical

Table 5. Pearson-statistics parameters.

$d - L_{\rm broad}$		$d - {\rm SH}$	
r	p-value	r	p-value
0.85	0.40	0.96	0.14

Notes. The first column refers to the correlation between density and X-ray luminosity in the broad band (0.5–7 KeV) and the second to the relation between the density and the colour $\log_{10}({\rm S/H})$, where S is the soft band (0.5–1.2 KeV) and H the hard band (2–7 keV). In both cases, r indicates the correlation coefficient.

and X-ray-emitting SNRs in NGC 4212, NGC 2403, and NGC 3077, where they also found no correlation. They support the idea that a non-uniform ISM, along with the coexistence of different materials at varying temperatures, likely contributes to the observed lack of correlation. In addition to a non-uniform ISM, the absence of correlation could also be influenced by the evolutionary phase of the SNRs. Younger SNRs are expected to exhibit stronger X-ray emission, whereas older SNRs tend to have stronger optical emission. To accurately examine these correlations, larger sample sizes are needed.

4.8. Comparison with X-ray SNRs in other nearby galaxies

In this section, we compare our results with those of other galaxies. More specifically, in Table 6, we list galaxies within 10 Mpc for which X-ray SNRs, identified as counterparts to optical SNRs, have been reported, along with their distance, SFR (based on the Hα luminosity of the galaxy), number of optical SNRs, number of X-ray SNRs, and the minimum X-ray luminosity of the X-ray SNRs. In general, more X-ray SNRs have been reported in these galaxies based on their soft emission and/or X-ray spectra; however, for consistency, we only consider those that have also been identified in the optical, and with the diagnostic [S II]/Hα $>$ 0.4. We applied this optical criterion for consistency, as optical SNRs in most of these galaxies have historically been selected based on this same criterion.

The purpose of this comparison is to estimate the expected number of X-ray SNRs in NGC 7793 and to identify the factors that may hinder their detection. We acknowledge that an objective comparison is not possible due to various biases. The most fundamental biases include variations in exposure times across surveys and differences in instrument sensitivities. In addition, there are cases where the X-ray data do not cover the entire galaxy. In addition, a low-density ISM/CSM, for example, resulting from low-metallicity stars with low mass-loss rates, could lead to non-detection.

Examining the quantities presented in Table 6, we do not find any strong correlations among them. In Figure 9, we show the number of X-ray SNRs identified in the galaxy sample as a function of their SFR. The distance is shown in the colour bar. We observe a trend in which galaxies with higher SFRs, such as NGC 3077, NGC 4214, M31, LMC, and M33, tend to have a greater number of X-ray SNRs. These, along with SMC, are the nearest galaxies. However, M51, M101, M74, NGC 2403, NGC 7793, and NGC 6946 do not follow this trend. Surprisingly, M101, M51, and NGC 6946, which have significantly higher SFRs than the rest of the galaxies, present a relatively low number of X-ray SNRs. This is probably an indication that distance is a significant barrier to identifying X-ray SNRs, although we cannot make quantitative conclusions due to the biases mentioned earlier.

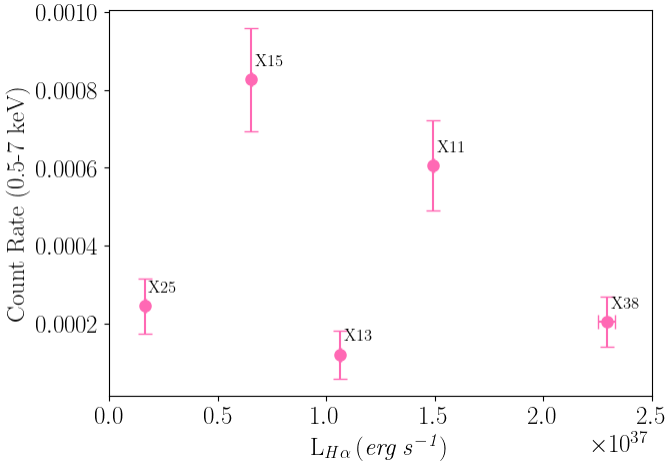

Fig. 8. Absorption-corrected *Chandra* X-ray luminosity in the broad band (0.5–7 keV) of the X-ray SNRs suggested in this study, as a function of their Hα luminosity.

In Figure 10, we present the number of X-ray SNRs versus the number of optical SNRs. There is a trend in which galaxies with more optical SNRs tend to have more X-ray SNRs. This is expected; however, the galaxies M74, SMC, and LMC deviate from this trend, forming a 'parallel branch'. The biases affecting optical studies are even more pronounced since, in addition to the aforementioned factors, there is a significant variation in optical instruments and, consequently, in the sensitivity of the observations. This is also reflected in the fact that no correlation appears between the number of optical SNRs and SFR. Despite the biases mentioned earlier, expanding the sample of galaxies would allow us to draw more accurate qualitative conclusions and better understand the factors influencing the detection of X-ray SNRs.

5. Conclusions

In this study, we analysed all archival *Chandra* observations of the galaxy NGC 7793 to detect X-ray SNRs, in addition to the single X-ray SNR previously known in this galaxy, primarily comparing with already known optical SNRs. Our main findings are listed below.

1. We detect five X-ray SNRs (X11, X15, X13, X25, X38), four of which are newly identified. These sources are considered X-ray SNRs primarily because they have optical SNR counterparts. Additional factors supporting this classification include:
   a The presentation of soft X-ray emission, positioning them in the soft region of the colour-colour diagrams.
   b The lack of significant short- or long-term variability.
   c The modelling of combined *XMM-Newton* EPIC MOS spectra (1.1 Ms) for X11 and X15 reveal soft emission typical of hot plasma ($T > 2.5{\times}10^6$ K) with strong O VII, O VIII, and Ne IX K-shell lines.

   We also explored correlations between the X-ray and optical properties of SNRs. We find that all X-ray SNRs exhibit strong [O III](5007Å) emission and that there are positive correlations between X-ray luminosity and pre-shock density (calculated using the [S II](6717)/[S II](6731) ratio), as well as between colour ($\log_{10}$(S/H)) and pre-shock density. However, although these trends are theoretically predicted,

Table 6. Information on galaxies with X-ray SNRs.

Name	Distance (Mpc)	SFR ($M_\odot\,yr^{-1}$)	$N_{optical}$	N_{Xrays}	Lx_{min} ($\times10^{35}$ erg s^{-1})
NGC 7793	3.70[1a]	0.51[1b,1c]	55[1d]	5*	8.8*
LMC	0.05[2a]	0.35[1b,1c]	49[2b]	70[2c,2d]	0.08[2c,2d]
SMC	0.06[3a]	0.19[1b,1c]	20[3b]	17[3b]	0.05[3b]
M31	0.68[4a]	0.27[1b,1c]	156[4b]	23[4c]	120[4c]
M33	0.80[5a]	0.45[1b,1c]	216[5b,5c]	112[5d]	0.16[5d]
NGC 4214	2.70[6a]	0.12[1b,1c]	92[6b]	7[6b,6c]	25[6c]
NGC 2403	3.06[7a]	0.48[1b,1c]	109[6b]	9[6b,6c]	25[6c]
NGC 3077	3.81[8a]	0.05[1b,1c]	18[6b]	1[6b,6c]	400[6c]
NGC 6946	5.37[9a]	2.28[1b,1c]	157[9b]	6[9c]	65[9c]
M101	7.2[10a]	1.41[1b,1c]	93[10b]	7[9c]	19[9c]
M51	8.58[11a]	1.5[1b,1c]	179[11b]	55[11b]	11.1[11b]
M74	9.59[12a]	0.59[1b,1c]	9[12b]	3[12b]	500[12b]

Notes. [(1a)] Radburn-Smith et al. (2011) [(1b)] Kennicutt et al. (2008) [(1c)] Lee et al. (2009) [(1d)] Kopsacheili et al. (2021) [(*)] This work (*XMM-Newton*) [(2a)] Pietrzyński et al. (2019) [(2b)] Yew et al. (2021) [(2c)] Zangrandi et al. (2024) [(2d)] Sasaki et al. (2025) [(3a)] Groenewegen (2013) [(3b)] Maggi et al. (2019) [(4a)] Clementini & Contreras (2011) [(4b)] Lee & Lee (2014a) [(4c)] Sasaki et al. (2012) [(5a)] Lee et al. (2002) [(5b)] Long et al. (2010) [(5c)] Lee & Lee (2014b) [(5d)] Garofali et al. (2017) [(6a)] Lelli et al. (2014) [(6b)] Leonidaki et al. (2013) [(6c)] Leonidaki et al. (2010) [(7a)] Tammann et al. (2008) [(8a)] Tully et al. (2013) [(9a)] Rodríguez et al. (2014) [(9b)] Long et al. (2019) [(9c)] Pannuti et al. (2007) [(10a)] Sabbi et al. (2018) [(10b)] Matonick & Fesen (1997) [(11a)] McQuinn et al. (2017) [(11b)] Winkler et al. (2021) [(12a)] Kreckel et al. (2017) [(12b)] Sonbaş et al. (2010).

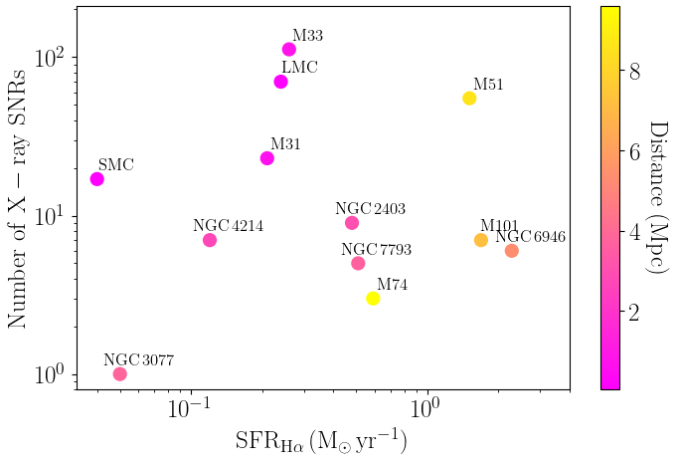

Fig. 9. Number of X-ray SNRs, counterparts of optical SNRs with [S II]/Hα > 0.4, as a function of their Hα SFR. The colour bar indicates the distance of the galaxies.

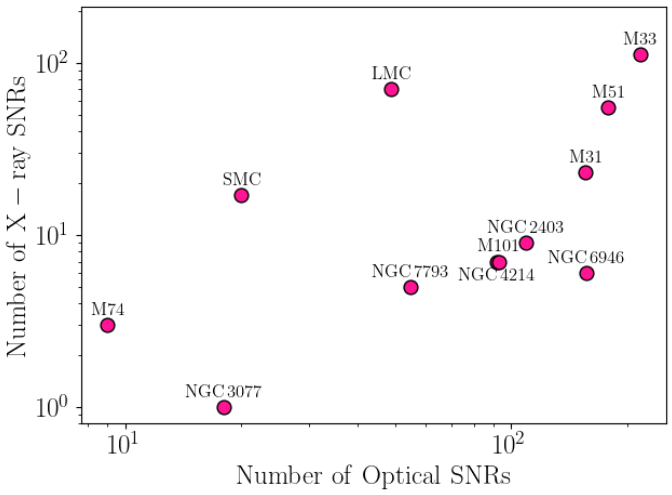

Fig. 10. Number of X-ray SNRs, counterparts of optical SNRs with [S II]/Hα > 0.4, versus the number of optical SNRs.

larger samples are required to confirm them with greater accuracy.

2. We report X-ray emission from SN 2008bk and refine its position.
3. We suggest two new candidate X-ray SNRs (X23 and X42). Although they have not been detected in optical wavelengths, we classify them as SNR candidates due to their soft, non-variable X-ray emission. Notably, for one of them (X42), the modelling of the combined *XMM-Newton* EPIC MOS spectrum revealed soft emission from hot plasma ($T > 2.5 \times 10^6$ K) with strong K-shell emission lines of O VII, O VIII, and Ne IX, similar to the X-ray SNRs with optical SNR counterparts reported in this study.
4. Finally, we compare our results with those from studies of nearby galaxies where SNR populations have been examined in optical and X-ray wavelengths. We propose that distance, in combination with the limited sensitivity of the instruments, is a significant factor in not detecting as many SNRs as expected based on the SFR of the galaxies.

With this study, we significantly increase the number of known X-ray SNRs in NGC 7793 from one to five. Additionally, this work contributes to the study of X-ray SNRs beyond the Local Group, where only a few have been identified. Systematic investigations of their properties require larger samples. Advances in optical identification techniques pave the way for detecting more optical SNRs, thereby increasing the likelihood of identifying additional X-ray counterparts.

Data availability

For this work we used archival data from *Chandra* and *XMM-Newton* telescopes.

Acknowledgements. We thank the anonymous referee for the thorough review and the useful comments that helped to improve the clarity of the paper. MK acknowledges financial support from MICINN (Spain) through the programme Juan de la Cierva-Incorporación [JC2022-049447-I]. MK and LG acknowledge financial support from AGAUR, CSIC, MCIN and AEI 10.13039/501100011033 under projects PID2023-151307NB-I00, PIE 20215AT016, Unidad de Excelencia María de Maeztu CEX2020-001058-M, and 2021-SGR-01270. KA acknowledges support from *Chandra* grants GO3-24033B, GO0-21010X, and TM9-20001X, and *JWST* grant JWST-GO-01905.002-A. KA also made use of NASA's Astrophysics Data System Bibliographic Services. NR is supported by the European Research Council (ERC) via the Consolidator Grant "MAGNESIA" (No. 817661) and the Proof of Concept "DeepSpacePulse" (No. 101189496), by the Catalan grant SGR2021-01269 (PI: Graber/Rea), the Spanish grant ID2023-153099NA-I00 (PI Coti Zelati), and by the program Unidad de Excelencia Maria de Maeztu CEX2020-001058-M. CPG acknowledges financial support from the Secretary of Universities and Research (Government of Catalonia) and by the Horizon 2020 Research and Innovation Programme of the European Union under the Marie Skłodowska-Curie and the Beatriu de Pinós 2021 BP 00168 programme, from the Spanish Ministerio de Ciencia e Innovación (MCIN) and the Agencia Estatal de Investigación (AEI) 10.13039/501100011033 under the PID2020-115253GA-I00 HOSTFLOWS project, and the program Unidad de Excelencia María de Maeztu CEX2020-001058-M.

References

Albert, C., & Dwarkadas, V. V. 2022, MNRAS, 514, 728
Anastasopoulou, K., Ponti, G., Sormani, M. C., et al. 2023, A&A, 671, A55
Arnaud, K. A. 1996, ASPC, 101, 17
Blair, W. P., & Long, K. S. 1997, ApJS, 108, 261
Boumis, P., Chiotellis, A., Fragkou, V., et al. 2022, MNRAS, 512, 1658
Bozzetto, L. M., Filipović, M. D., Vukotić, B., et al. 2017, ApJS, 230, 2
Brightman, M., Hameury, J.-M., Lasota, J., et al. 2023, ApJ, 951, 51
Chen, Y., Seward, F. D., Sun, M., & Li, J. 2008, ApJ, 676, 1040
Chevalier, R. A. 1975, ApJ, 200, 698
Chevalier, R. A. 1982, ApJ, 259, 302
Chiotellis, A., Zapartas, E., & Meyer, D. M.-A. 2024, MNRAS, 531, 5109
Churazov, E. M., Khabibullin, I. I., Bykov, A. M., et al. 2021, MNRAS, 507, 971
Churazov, E. M., Khabibullin, I. I., Bykov, A. M., et al. 2022, MNRAS, 513, L83
Cid Fernandes, R., Carvalho, M. S., Sánchez, S. F., de Amorim, A., & Ruschel-Dutra, D. 2021, MNRAS, 502, 1386
Cioffi, D. F., McKee, C. F., & Bertschinger, E. 1988, ApJ, 334, 252
Clementini, G., Contreras, Ramos R., et al. 2011, ApJ, 743, 19
Cox, D. P., Shelton, R. L., Maciejewski, W., et al. 1999, ApJ, 524, 179
Davoust, E., & de Vaucouleurs, G. 1980, ApJ, 242, 30
Della, Bruna L., Adamo, A., Bik, A., et al. 2020, A&A, 635, A134
Dessart, L., Gutiérrez, C. P., Kuncarayakti, H., Fox, O. D., & Filippenko, A. V. 2023, A&A, 675, A33
Dopita, M. A., Payne, J. L., Filipović, M. D., & Pannuti, T. G. 2012, MNRAS, 427, 956
Draine, B. T. 2011, Physics of the Interstellar and Intergalactic Medium (Princeton University Press)
Dwarkadas, V. V. 2005, ApJ, 630, 892
Evans, I. N., Primini, F. A., Glotfelty, K. J., et al. 2010, ApJS, 189, 37
Fesen, R. A., Drechsler, M., Weil, K. E., et al. 2021, ApJ, 920, 90
Filipović, M. D., Haberl, F., Winkler, P. F., et al. 2008, A&A, 485, 63
Filippenko, A. V. 1997, ARA&A, 35, 309
Freeman, P. E., Kashyap, V., Rosner, R., & Lamb, D. Q. 2002, ApJS, 138, 185
Fruscione, A., McDowell, J. C., Allen, G. E., et al. 2006, SPIE, 6270, 62701V
Galvin, T. J., & Filipovic, M. D. 2014, SerAJ, 189, 15
Garmire, G. P. 1997, Bull. Am. Astron. Soc., 29, 823
Garofali, K., Williams, B. F., Plucinsky, P. P., et al. 2017, MNRAS, 472, 308
Groenewegen, M. A. T. 2013, A&A, 550, A70
Haberl, F., Sturm, R., Ballet, J., et al. 2012, A&A, 545, A128
Hodge, P. W. 1969, ApJS, 18, 73
Kennicutt, R. C., Lee, J. C., Funes, J. G., et al. 2008, ApJS, 178, 247
Kopsacheili, M., Zezas, A., & Leonidaki, I. 2020, MNRAS, 491, 889
Kopsacheili, M., Zezas, A., Leonidaki, I., & Boumis, P. 2021, MNRAS, 507, 6020
Kopsacheili, M., Zezas, A., & Leonidaki, I. 2022, MNRAS, 514, 3260
Kopsacheili, M., Jiménez-Palau, C., Galbany, L., Boumis, P., & González-Díaz, R. 2024, MNRAS, 530, 1078
Kreckel, K., Groves, B., Bigiel, F., et al. 2017, ApJ, 834, 174
Lee, J. H., & Lee, M. G. 2014a, ApJ, 786, 130
Lee, J. H., & Lee, M. G. 2014b, ApJ, 793, 134
Lee, M. G., Kim, M., Sarajedini, A., Geisler, D., & Gieren, W. 2002, ApJ, 565, 959
Lee, J. C., Gil de Paz, A., Tremonti, C., et al. 2009, ApJ, 706, 599
Lelli, F., Verheijen, M., & Fraternali, F. 2014, A&A, 566, A71
Leonidaki, I., Zezas, A., & Boumis, P. 2010, ApJ, 725, 842
Leonidaki, I., Boumis, P., & Zezas, A. 2013, MNRAS, 429, 189
Li, W., van Dyk, S. D., Filippenko, A. V., et al. 2008, ATel, 1448, 1
Long, K. S., Blair, W. P., Winkler, P. F., et al. 2010, ApJS, 187, 495
Long, K. S., Winkler, P. F., & Blair, W. P. 2019, ApJ, 875, 85
Maggi, P., Filipović, M. D., Vukotić, B., et al. 2019, A&A, 631, A127
Matonick, D. M., & Fesen, R. A. 1997, ApJS, 112, 49
Mattila, S., Smartt, S. J., Eldridge, J. J., et al. 2008, ApJ, 688, L91
Maund, J. R., Mattila, S., Ramirez-Ruiz, E., & Eldridge, J. J. 2014, MNRAS, 438, 1577
McQuinn, K. B. W., Skillman, E. D., Dolphin, A. E., Berg, D., & Kennicutt, R. 2017, AJ, 154, 51
Milisavljevic, D., & Fesen, R. A. 2013, ApJ, 772, 134
Mineo, S., Gilfanov, M., & Sunyaev, R. 2012, MNRAS, 419, 2095
Misra, K., Pooley, D., Chandra, P., et al. 2007, MNRAS, 381, 280
Monet, D. G., Levine, S. E., Canzian, B., et al. 2003, AJ, 125, 984
Motch, C., Pakull, M. W., Grisé, F., & Soria, R. 2011, AN, 332, 367
O'Dell, S. L., Swartz, D. A., Tice, N. W., et al. 2015, SPIE, 9601, 960107
Osterbrock, D. E., & Ferland, G. J. 2006, Astrophysics of gaseous nebulae and active galactic nuclei, 2nd. ed. (Sausalito, CA: University Science Books)
Pakull, M. W., Soria, R., & Motch, C. 2010, Nature, 466, 209
Palaiologou, E. V., Leonidaki, I., & Kopsacheili, M. 2022, MNRAS, 515, 339
Pannuti, T. G., Duric, N., Lacey, C. K., et al. 2002, ApJ, 565, 966
Pannuti, T. G., Schlegel, E. M., & Lacey, C. K. 2007, AJ, 133, 1361
Pannuti, T., Chomiuk, L., Grimes, C. K., et al. 2011, AAS Meeting, 217, 256.33
Pannuti, T. G., Schlegel, E. M., Filipović, M. D., et al. 2011, AJ, 142, 20
Park, T., Kashyap, V. L., Siemiginowska, A., et al. 2006, ApJ, 652, 610
Pietrzyński, G., Graczyk, D., Gallenne, A., et al. 2019, Natur, 567, 200
Pooley, D., Lewin, W. H. G., Fox, D. W., et al. 2002, ApJ, 572, 932
Puche, D., & Carignan, C. 1988, AJ, 95, 1025
Radburn-Smith, D. J., de Jong, R. S., Seth, A. C., et al. 2011, ApJS, 195, 18
Raymond, J. C. 1979, ApJS, 39, 1
Read, A. M., & Pietsch, W. 1999, A&A, 341, 8
Rho, J., Petre, R., Schlegel, E. M., & Hester, J. J. 1994, ApJ, 430, 757
Rodríguez, Ó., Clocchiatti, A., & Hamuy, M. 2014, AJ, 148, 107
Sabbi, E., Calzetti, D., Ubeda, L., et al. 2018, ApJS, 235, 23
Safi-Harb, S., & Petre, R. 1999, ApJ, 512, 784
Sasaki, M., Gaetz, T. J., Blair, W. P., et al. 2006, ApJ, 642, 260
Sasaki, M., Pietsch, W., Haberl, F., et al. 2012, A&A, 544, A144
Sasaki, M., Zangrandi, F., Filipović, M., et al. 2025, A&A, 693, L15
Shelton, R. L., Cox, D. P., Maciejewski, W., et al. 1999, ApJ, 524, 192
Smith, R. K., Brickhouse, N. S., Liedahl, D. A., & Raymond, J. C. 2001, ApJ, 556, L91
Sonbaş, E., Akyüz, A., Balman, Ş., & Özel, M. E. 2010, A&A, 517, A91
Soria, R., Pakull, M. W., Broderick, J. W., Corbel, S., & Motch, C. 2010, MNRAS, 409, 541
Tammann, G. A., Sandage, A., & Reindl, B. 2008, A&ARv, 15, 289
Temim, T., Slane, P., Raymond, J. C., et al. 2022, ApJ, 932, 26
Tully, R. B., Courtois, H. M., Dolphin, A. E., et al. 2013, AJ, 146, 86
Van Dyk, S. D. 2013, AJ, 146, 24
Van Dyk, S. D., Davidge, T. J., Elias-Rosa, N., et al. 2012, AJ, 143, 19
Vink, J. 2012, A&ARv, 20, 49
Vink, J. 2020, Physics and Evolution of Supernova Remnants, Astronomy and Astrophysics Library (Springer Nature Switzerland AG)
Weisskopf, M. C., Tananbaum, H. D., Van Speybroeck, L. P., & O'Dell, S. L. 2000, SPIE, 4012, 2
White, R. L., & Long, K. S. 1991, ApJ, 373, 543
Williams, B. J., Katsuda, S., Cumbee, R., et al. 2020, ApJ, 898, L51
Wilms, J., Allen, A., & McCray, R. 2000, ApJ, 542, 914
Winkler, P. F., Coffin, S. C., Blair, W. P., Long, K. S., & Kuntz, K. D. 2021, ApJ, 908, 80
Yew, M., Filipović, M. D., Stupar, M., et al. 2021, MNRAS, 500, 2336
Zangrandi, F., Jurk, K., Sasaki, M., et al. 2024, A&A, 692, A237
Zhang, G.-Y., Chen, Y., Su, Y., et al. 2015, ApJ, 799, 103

Appendix A: Properties of the *Chandra* detected sources

Table A.1. Detected *Chandra* sources in NGC 7793 and their X-ray properties.

ID	RA (J2000)	DEC (J2000)	ncr broad ($\times10^{-5}$) 0.5 - 7.0 keV	ncr soft ($\times10^{-5}$) 0.5 - 1.2 keV	ncr medium ($\times10^{-5}$) 1.2 - 2.0 keV	ncr hard ($\times10^{-5}$) 2.0 - 7.0 keV	S/N_{broad}	S/N_{soft}
X1	23:57:35.0	-32:27:54.3	97.66 ± 13.86	28.14 ± 7.20	29.87 ± 7.40	39.65 ± 9.25	5.88	2.87
X2	23:57:36.5	-32:38:44.9	85.34 ± 13.70	35.93 ± 8.27	26.80 ± 7.37	22.62 ± 8.06	5.08	3.29
X3	23:57:36.8	-32:29:26.6	70.93 ± 12.33	24.23 ± 6.48	28.46 ± 7.47	18.24 ± 7.37	4.64	2.70
X4	23:57:38.7	-32:30:45.5	8.88 ± 5.24	1.73 ± 1.73	3.06 ± 3.24	4.08 ± 3.74	1.04	0.34
X5	23:57:39.0	-32:39:08.6	274.33 ± 30.56	40.42 ± 11.67	94.32 ± 17.82	139.59 ± 21.91	7.89	2.43
X6	23:57:42.7	-32:37:17.2	46.87 ± 9.88	7.46 ± 4.38	20.39 ± 5.89	19.01 ± 6.61	3.69	1.00
X7	23:57:43.2	-32:33:56.6	32.00 ± 7.89	8.66 ± 3.87	10.39 ± 4.24	12.96 ± 5.41	3.03	1.29
X8	23:57:43.5	-32:29:28.4	43.85 ± 9.56	5.51 ± 3.60	11.41 ± 4.63	26.93 ± 7.54	3.54	0.82
X9	23:57:43.8	-32:36:34.7	273.53 ± 22.31	84.05 ± 12.38	101.50 ± 13.33	87.97 ± 12.92	11.04	5.67
X10	23:57:43.9	-32:34:21.8	44.27 ± 9.14	18.69 ± 5.64	21.26 ± 6.18	4.31 ± 3.69	3.78	2.29
X11	23:57:44.0	-32:34:40.9	60.62 ± 11.49	62.44 ± 11.41	0.00 ± 0.00	-1.82 ± 1.29	4.20	4.39
X12	23:57:44.1	-32:28:43.3	374.64 ± 25.92	139.19 ± 15.74	141.26 ± 15.69	94.19 ± 13.34	13.27	7.72
X13	23:57:45.8	-32:35:01.5	12.05 ± 6.17	9.14 ± 4.69	0.97 ± 2.31	1.94 ± 3.27	1.23	1.12
X14	23:57:46.8	-32:36:07.7	954.90 ± 44.50	335.37 ± 26.40	313.73 ± 25.38	305.80 ± 25.28	20.33	11.59
X15	23:57:47.3	-32:35:23.5	82.62 ± 13.37	79.60 ± 13.01	4.09 ± 2.89	-1.07 ± 1.07	5.09	5.03
X16	23:57:48.2	-32:36:57.8	73.17 ± 11.86	45.35 ± 9.08	13.06 ± 5.26	14.76 ± 5.53	5.05	3.92
X17	23:57:48.5	-32:28:51.5	63.10 ± 11.34	22.80 ± 6.56	28.71 ± 7.17	11.58 ± 5.84	4.47	2.47
X18	23:57:48.7	-32:32:33.7	68.55 ± 12.21	37.83 ± 8.96	28.61 ± 7.65	2.10 ± 3.21	4.53	3.17
X19	23:57:49.9	-32:35:28.3	2636.44 ± 167.34	452.08 ± 67.39	1092.18 ± 108.31	1092.18 ± 108.31	14.85	5.64
X20	23:57:50.5	-32:33:20.3	27.12 ± 7.23	15.22 ± 5.66	6.80 ± 3.40	5.10 ± 2.94	2.79	1.84
X21	23:57:51.0	-32:42:54.5	77.50 ± 18.87	6.74 ± 4.76	37.73 ± 11.82	33.04 ± 13.92	3.11	0.62
X22	23:57:51.1	-32:37:26.9	13341.46 ± 165.91	4269.22 ± 93.75	4103.96 ± 92.00	4968.28 ± 101.36	79.21	44.41
X23	23:57:51.2	-32:36:00.7	65.33 ± 10.86	66.21 ± 10.82	0.00 ± 0.00	-0.88 ± 0.88	4.93	5.03
X24	23:57:51.9	-32:33:38.7	16.91 ± 6.31	4.09 ± 2.89	4.09 ± 2.89	8.74 ± 4.80	1.77	0.62
X25	23:57:52.2	-32:34:13.8	24.52 ± 7.08	22.48 ± 6.78	2.04 ± 2.04	0.00 ± 0.00	2.43	2.29
X26	23:57:52.8	-32:33:09.9	578.29 ± 34.38	183.91 ± 19.39	222.73 ± 21.33	171.65 ± 18.73	15.77	8.42
X27	23:57:53.1	-32:42:23.6	123.12 ± 21.30	1.99 ± 3.64	73.35 ± 16.33	47.78 ± 13.19	4.67	0.19
X28	23:57:53.3	-32:28:12.2	3438.21 ± 77.72	1611.35 ± 53.18	1085.82 ± 43.54	741.05 ± 36.28	43.03	29.14
X29	23:57:54.1	-32:31:35.0	35.64 ± 8.74	14.30 ± 5.41	7.03 ± 4.24	14.30 ± 5.41	3.04	1.66
X30	23:57:54.9	-32:39:55.9	151.89 ± 16.39	59.90 ± 10.24	59.48 ± 10.05	32.51 ± 7.92	8.12	4.76
X31	23:57:56.2	-32:36:33.1	60.41 ± 10.43	19.57 ± 5.94	24.67 ± 6.63	16.17 ± 5.44	4.70	2.29
X32	23:57:56.2	-32:31:37.1	15.58 ± 5.19	5.19 ± 3.00	3.46 ± 2.45	6.92 ± 3.46	1.99	0.86
X33	23:57:56.4	-32:34:45.9	23.98 ± 6.75	3.40 ± 2.40	13.59 ± 4.81	6.99 ± 4.09	2.58	0.62
X34	23:57:56.5	-32:36:00.3	149.94 ± 17.85	55.56 ± 10.94	59.26 ± 11.00	35.12 ± 8.83	7.32	4.03
X35	23:57:56.7	-32:27:50.0	34.97 ± 15.53	7.33 ± 7.54	12.14 ± 7.01	15.50 ± 11.63	1.51	0.48
X36	23:57:57.5	-32:31:49.5	22.50 ± 6.24	3.46 ± 2.45	8.66 ± 3.87	10.39 ± 4.24	2.57	0.62
X37	23:57:57.9	-32:26:46.8	31.24 ± 9.96	20.97 ± 6.64	9.08 ± 4.34	1.20 ± 6.03	2.31	2.20
X38	23:57:59.2	-32:36:06.6	20.43 ± 6.46	12.26 ± 5.01	6.13 ± 3.54	2.04 ± 2.04	2.14	1.48
X39	23:57:59.9	-32:32:41.1	185.27 ± 20.39	80.38 ± 13.52	61.30 ± 11.19	43.59 ± 10.37	8.13	4.99
X40	23:57:59.9	-32:33:20.2	18.39 ± 11.00	-2.04 ± 8.91	10.22 ± 4.57	10.22 ± 4.57	1.58	-0.23
X41	23:58:00.2	-32:33:26.0	94.34 ± 13.21	76.17 ± 11.48	19.04 ± 5.74	-0.87 ± 3.12	6.13	5.56
X42	23:58:00.4	-32:34:54.8	124.65 ± 15.96	114.43 ± 15.29	10.22 ± 4.57	0.00 ± 0.00	6.74	6.41
X43	23:58:00.7	-32:32:39.5	25.5 ± 8.69	6.82±4.75	10.91±5.56	7.79 ±4.70	2.03	0.79
X44	23:58:02.9	-32:36:14.8	230.04 ± 19.85	83.27 ± 11.90	68.61 ± 10.93	78.17 ± 11.53	10.51	5.93
X45	23:58:03.5	-32:36:44.2	152.79 ± 17.90	69.48 ± 11.92	45.74 ± 9.88	37.57 ± 9.00	7.44	4.76
X46	23:58:05.5	-32:32:50.8	10.22 ± 5.60	2.55 ± 3.02	6.13 ± 4.21	1.53 ± 2.11	1.08	0.36
X47	23:58:06.7	-32:37:57.0	1558.32 ± 56.89	631.49 ± 36.18	527.25 ± 33.01	399.57 ± 28.95	26.24	16.34
X48	23:58:07.4	-32:26:06.5	53.15 ± 12.27	13.04 ± 5.35	23.72 ± 7.39	16.39 ± 8.21	3.35	1.56
X49	23:58:07.8	-32:37:15.9	22.46 ± 7.07	11.11 ± 4.56	7.71 ± 3.88	3.65 ± 3.75	2.26	1.51
X50	23:58:07.9	-32:36:15.1	49.04 ± 10.01	18.39 ± 6.13	12.26 ± 5.01	18.39 ± 6.13	3.83	1.99
X51	23:58:08.4	-32:38:48.0	237.13 ± 20.81	29.25 ± 7.27	83.33 ± 12.23	124.54 ± 15.18	10.18	2.98
X52	23:58:08.8	-32:34:03.8	3709.19 ± 80.51	1751.79 ± 55.27	1246.32 ± 46.68	711.08 ± 35.33	44.99	30.63
X53	23:58:09.7	-32:36:17.3	146.08 ± 15.90	39.08 ± 8.15	67.09 ± 10.78	39.90 ± 8.37	8.09	3.73
X54	23:58:10.5	-32:33:57.6	281.99 ± 24.18	94.00 ± 13.86	110.35 ± 15.29	77.65 ± 12.60	10.59	5.71
X55	23:58:10.7	-32:41:22.0	29.60 ± 14.06	-0.55 ± 4.06	6.18 ± 6.26	23.98 ± 11.91	1.43	-0.05
X56	23:58:11.3	-32:33:26.3	59.48 ± 10.05	18.69 ± 5.64	28.89 ± 7.01	11.90 ± 4.50	4.84	2.29
X57	23:58:14.2	-32:29:03.5	45.61 ± 9.71	15.58 ± 5.19	22.13 ± 6.59	7.90 ± 4.89	3.64	1.99
X58	23:58:15.8	-32:31:09.2	52.13 ± 9.70	17.31 ± 5.47	24.23 ± 6.48	10.58 ± 4.71	4.29	2.14

Appendix B: Colors of the X-ray detected sources

Table B.1. Colors and the corresponding OBSIDs of the detected sources

ID	OBSID	$\log_{10}$(S/H)	$\log_{10}$(S/M)	$\log_{10}$(M/H)	Other Surveys
X1	13439	$-0.07^{+0.16}_{-0.15}$	$0.06^{+0.15}_{-0.16}$	$-0.14^{+0.16}_{-0.13}$	
X2	14231	$0.24^{+0.22}_{-0.16}$	$0.20^{+0.14}_{-0.18}$	$0.09^{+0.20}_{-0.21}$	
X3	13439	$0.26^{+0.21}_{-0.24}$	$0.03^{+0.16}_{-0.16}$	$0.21^{+0.23}_{-0.22}$	
X4	13439	$-0.20^{+0.74}_{-0.73}$	$-0.08^{+0.74}_{-0.80}$	$-0.14^{+0.84}_{-0.72}$	
X5	23266	$-0.38^{+0.14}_{-0.15}$	$-0.25^{+0.13}_{-0.17}$	$-0.13^{+0.11}_{-0.10}$	
X6	14231	$-0.39^{+0.37}_{-0.31}$	$-0.38^{+0.30}_{-0.34}$	$0.04^{+0.21}_{-0.20}$	
X7	13439	$-0.05^{+0.31}_{-0.27}$	$0.03^{+0.27}_{-0.28}$	$-0.04^{+0.26}_{-0.30}$	
X8	13439	$-0.66^{+0.36}_{-0.34}$	$-0.20^{+0.29}_{-0.49}$	$-0.32^{+0.19}_{-0.26}$	
X9	14231	$0.00^{+0.09}_{-0.09}$	$-0.07^{+0.09}_{-0.09}$	$0.08^{+0.08}_{-0.09}$	J235743.8-323633$^{(p)}$
X10	14231	$0.57^{+0.57}_{-0.32}$	$0.00^{+0.16}_{-0.21}$	$0.63^{+0.51}_{-0.38}$	
X11	3954	$1.84^{+0.92}_{-0.60}$	$2.00^{+0.76}_{-0.76}$	$-0.13^{+1.32}_{-1.03}$	7793_24$^{(k1)}$, SNR_91$^{(k2)}$, J235743.9-323441$^{(mn)}$
X12	13439	$0.18^{+0.07}_{-0.08}$	$0.01^{+0.06}_{-0.07}$	$0.19^{+0.07}_{-0.09}$	P5$^{(r)}$
X13	3954	$0.47^{+0.78}_{-0.56}$	$0.73^{+0.74}_{-0.66}$	$-0.26^{+1.04}_{-0.90}$	7793_23$^{(k1)}$, SNR_126$^{(k2)}$
X14	3954	$0.03^{+0.05}_{-0.05}$	$0.03^{+0.05}_{-0.05}$	$0.00^{+0.04}_{-0.06}$	J235746.7-323607$^{(p)}$, SNR R3$^{(pr)}$
X15	3954	$1.88^{+0.96}_{-0.56}$	$1.22^{+0.41}_{-0.31}$	$0.81^{+0.86}_{-0.93}$	S11$^{(b97,pr)}$, 7793_22$^{(k1)}$, J235747.2-323523$^{(p)}$, SNR_136$^{(k2)}$
X16	14231	$0.49^{+0.19}_{-0.20}$	$0.55^{+0.19}_{-0.22}$	$-0.05^{+0.25}_{-0.26}$	
X17	13439	$0.26^{+0.33}_{-0.24}$	$-0.08^{+0.15}_{-0.18}$	$0.39^{+0.28}_{-0.27}$	
X18	3954	$1.02^{+0.73}_{-0.41}$	$0.14^{+0.15}_{-0.16}$	$1.08^{+0.53}_{-0.60}$	H18$^{(h)}$, 0574-1250312$^{(u)}$, P6$^{(r)}$, J235748.6-323234$^{(p)}$
X19	27481	$-0.38^{+0.09}_{-0.07}$	$-0.39^{+0.09}_{-0.07}$	$0.01^{+0.06}_{-0.06}$	J235749.9-323526$^{(b)}$
X20	14231	$0.49^{+0.40}_{-0.36}$	$0.39^{+0.33}_{-0.35}$	$0.21^{+0.38}_{-0.53}$	SN 2008bk$^{(v)}$
X21	23266	$-0.58^{+0.42}_{-0.41}$	$-0.62^{+0.32}_{-0.42}$	$0.05^{+0.27}_{-0.22}$	P21$^{(r)}$
X22	3954	$-0.07^{+0.01}_{-0.01}$	$0.02^{+0.01}_{-0.01}$	$-0.09^{+0.01}_{-0.01}$	P13$^{(r)}$, J235750.9-323726$^{(p)}$
X23	14231	$1.89^{+0.96}_{-0.56}$	$2.12^{+0.75}_{-0.77}$	$0.05^{+1.14}_{-1.21}$	
X24	3954	$-0.29^{+0.48}_{-0.55}$	$-0.01^{+0.59}_{-0.58}$	$-0.28^{+0.48}_{-0.55}$	
X25	3954	$1.34^{+0.96}_{-0.59}$	$1.00^{+0.55}_{-0.53}$	$0.34^{+1.15}_{-0.89}$	J235752.2-323413$^{(p)}$, J235752.2-323413$^{(mn)}$, 7793_5$^{(k1)}$
X26	3954	$0.03^{+0.06}_{-0.07}$	$-0.09^{+0.07}_{-0.05}$	$0.11^{+0.07}_{-0.06}$	P7$^{(r)}$, 0574-1250339$^{(u)}$, J235752.7-323309$^{(p)}$
X27	23266	$-1.00^{+0.41}_{-0.81}$	$-1.27^{+0.46}_{-0.74}$	$0.19^{+0.16}_{-0.15}$	
X28	13439	$0.34^{+0.02}_{-0.03}$	$0.17^{+0.02}_{-0.02}$	$0.17^{+0.03}_{-0.03}$	P4$^{(r)}$
X29	3954	$0.01^{+0.27}_{-0.22}$	$0.31^{+0.37}_{-0.35}$	$-0.29^{+0.35}_{-0.35}$	
X30	14231	$0.23^{+0.13}_{-0.13}$	$0.01^{+0.10}_{-0.11}$	$0.23^{+0.13}_{-0.13}$	
X31	14231	$0.07^{+0.19}_{-0.21}$	$-0.10^{+0.18}_{-0.18}$	$0.15^{+0.20}_{-0.18}$	
X32	13439	$-0.17^{+0.56}_{-0.48}$	$0.13^{+0.69}_{-0.59}$	$-0.25^{+0.55}_{-0.64}$	
X33	14231	$-0.27^{+0.33}_{-0.58}$	$-0.53^{+0.35}_{-0.52}$	$0.31^{+0.34}_{-0.39}$	J235756.3-323444$^{(p)}$
X34	3954	$0.17^{+0.15}_{-0.14}$	$-0.04^{+0.12}_{-0.11}$	$0.20^{+0.15}_{-0.13}$	J235756.4-323559$^{(p)}$
X35	14378	$-0.25^{+0.68}_{-0.76}$	$-0.13^{+0.49}_{-0.70}$	$-0.11^{+0.55}_{-0.47}$	
X36	13439	$-0.44^{+0.45}_{-0.55}$	$-0.40^{+0.52}_{-0.53}$	$-0.06^{+0.34}_{-0.35}$	
X37	13439	$0.70^{+0.77}_{-0.52}$	$0.37^{+0.25}_{-0.28}$	$0.25^{+0.92}_{-0.47}$	
X38	3954	$0.69^{+0.58}_{-0.52}$	$0.24^{+0.41}_{-0.31}$	$0.36^{+0.70}_{-0.56}$	S24$^{(b98)}$, 7793_21$^{(k1)}$
X39	3954	$0.26^{+0.15}_{-0.12}$	$0.12^{+0.11}_{-0.12}$	$0.17^{+0.12}_{-0.15}$	J235759.8-323240$^{(p)}$
X40	3954	$-0.38^{+0.68}_{-0.99}$	$-0.38^{+0.68}_{-0.99}$	$0.05^{+0.54}_{-0.66}$	
X41	13439	$1.57^{+0.95}_{-0.40}$	$0.60^{+0.17}_{-0.15}$	$1.04^{+0.88}_{-0.51}$	P8$^{(r)}$, J235800.1-323325$^{(p)}$
X42	3954	$2.16^{+0.85}_{-0.66}$	$1.04^{+0.28}_{-0.22}$	$1.01^{+0.98}_{-0.70}$	J235800.3-323455$^{(p)}$
X43	14231	$0.01^{+0.10}_{-0.08}$	$0.09^{+0.09}_{-0.09}$	$-0.07^{+0.09}_{-0.10}$	J235802.8-323614$^{(p)}$
X44	14231	$0.01^{+0.10}_{-0.08}$	$0.09^{+0.09}_{-0.09}$	$-0.07^{+0.09}_{-0.10}$	
X45	3954	$0.26^{+0.14}_{-0.12}$	$0.19^{+0.12}_{-0.12}$	$0.07^{+0.15}_{-0.14}$	J235803.5-323643$^{(p)}$
X46	3954	$0.25^{+0.04}_{-0.04}$	$0.13^{+0.03}_{-0.04}$	$0.12^{+0.04}_{-0.04}$	J235806.6-323757$^{(m)}$
X47	13439	$0.02^{+0.34}_{-0.32}$	$-0.15^{+0.21}_{-0.26}$	$0.13^{+0.37}_{-0.23}$	
X48	13439	$0.02^{+0.34}_{-0.32}$	$-0.16^{+0.21}_{-0.26}$	$0.13^{+0.37}_{-0.23}$	
X49	14231	$0.42^{+0.62}_{-0.44}$	$0.19^{+0.29}_{-0.33}$	$0.26^{+0.62}_{-0.53}$	
X50	3954	$0.04^{+0.19}_{-0.24}$	$0.20^{+0.24}_{-0.25}$	$-0.13^{+0.20}_{-0.29}$	J235807.8-323614$^{(p)}$
X51	14231	$-0.53^{+0.11}_{-0.13}$	$-0.36^{+0.11}_{-0.14}$	$-0.15^{+0.07}_{-0.10}$	
X52	13439	$0.41^{+0.02}_{-0.03}$	$0.16^{+0.02}_{-0.02}$	$0.25^{+0.03}_{-0.03}$	P9$^{(r)}$, J235808.7-323403$^{(p)}$
X53	14231	$0.03^{+0.14}_{-0.12}$	$-0.17^{+0.10}_{-0.13}$	$0.22^{+0.12}_{-0.11}$	J235807.8-323614$^{(p)}$
X54	3954	$0.07^{+0.11}_{-0.09}$	$-0.08^{+0.10}_{-0.08}$	$0.14^{+0.10}_{-0.09}$	J235810.4-323357$^{(p)}$
X55	23266	$-0.83^{+0.55}_{-1.00}$	$-0.39^{+0.89}_{-1.01}$	$-0.56^{+0.61}_{-0.56}$	
X56	14231	$0.20^{+0.26}_{-0.19}$	$-0.16^{+0.16}_{-0.19}$	$0.35^{+0.25}_{-0.16}$	
X57	13439	$0.51^{+0.35}_{-0.35}$	$0.03^{+0.16}_{-0.23}$	$0.43^{+0.42}_{-0.27}$	
X58	13439	$0.38^{+0.25}_{-0.25}$	$-0.04^{+0.19}_{-0.18}$	$0.41^{+0.22}_{-0.25}$	

Notes. $^{(p)}$Pannuti et al. (2011); $^{(k1)}$Kopsacheili et al. (2021); $^{(k2)}$Kopsacheili et al. (2024); $^{(mn)}$Mineo et al. (2012); $^{(r)}$Read & Pietsch (1999); $^{(pr)}$Pannuti et al. (2002); $^{(b97)}$Blair & Long (1997); $^{(h)}$Hodge (1969); $^{(u)}$USNO: Monet et al. (2003); $^{(m)}$Motch et al. (2011); $^{(b)}$Brightman et al. (2023); $^{(v)}$Van Dyk (2013)

Appendix C: X-ray sources unrelated to Supernova Remnants

In this section, we compare the detected sources that are unrelated to SNRs with those reported in previous studies. Source X18 had been misclassified as an H II region (H18; Hodge 1969), but as mentioned in Pannuti et al. (2011) (CXOUJ235748.6-323234) it is a foreground star (USNO 0574-1250312; Monet et al. 2003). This source has been earlier detected and labeled as P6 in Read & Pietsch (1999) by the ROSAT PSPC). Source X26 is also a foreground star (USNO 0574-1250339; Monet et al. 2003) and has been presented in Pannuti et al. 2011 as CXOU J235752.7-323309 and in Read & Pietsch (1999) as P7.

Source X41 (P8 in Read & Pietsch 1999; CXOU J235800.1-323325 in Pannuti et al. 2011) was first misclassified as SNR (S26 in Blair & Long 1997) but it is a microquasar (Pakull et al. 2010, Soria et al. 2010). According to Pannuti et al. (2011) the spatial extent in the X-ray, optical and radio wavelengths is similar. There is a super-bubble around this source (Kopsacheili et al. 2021) which is created by the microquasar (Dopita et al. 2012). X40 is also part of this bubble.

Source X52 is reported as CXOU J235808.7-323403 in Pannuti et al. (2011) and as P9 in Read & Pietsch (1999), both in X-rays. According to the latter it presents a soft spectrum, it is variable and highly absorbed. X22 is assumed to be either a background galaxy or a black-hole X-ray binary (CXOU J235750.9-323726 in Pannuti et al. 2011; P13 in Read & Pietsch 1999). Motch et al. (2011) identified a star with a V magnitude of 20.5 in the optical and suggested it as companion of this X-ray source. X46 is reported as variable and it is probably a X-ray binary (CXOU J235806.6-323757 in Motch et al. 2011). Source X19 coincides with the nuclear position of the galaxy (J235749.9-323526 in Brightman et al. 2023).

The sources X33 (CXOU J235756.3-323444), X34 (CXOU J235756.4-323559), X39 (CXOUJ235759.8-323240), X42 (CXOU J235800.3-323455), X43 (CXOU J235802.8-323614), X45 (CXOU J235803.5-323643), X50 (CXOU J235807.8-323614), X53 (CXOU J235809.6-323617), and X54 (CXOU J235810.4-323357) are presented in Pannuti et al. (2011) with their names indicated in the parenthesis. X12, X21, and X28 have been detected before by Read & Pietsch (1999) as P5, P21, and P4 respectively. X12 is reported as a faint source, X21 as a variable object associated to the galaxy, and X28 as a stellar object associated with the galaxy.